A TBX5-dependent compartment boundary patterns the cardiac interventricular septum

Irfan S. Kathiriya[1,#], Martin H. Dominguez[2,3], Kavitha S. Rao[1,2], Jonathon M. Muncie-Vasic[2], W. Patrick Devine[2,4], Kevin M. Hu[1,2], Swetansu K. Hota[2], Bayardo I. Garay[1], Diego Quintero[2], Piyush Goyal[1,2], Megan N. Matthews[1], Reuben Thomas[2], Tatyana Sukonnik[2], Dario Miguel-Perez[2], Sarah Winchester[2], Emily F. Brower[2], André Forjaz[5], Pei-Hsun Wu[5], Denis Wirtz[5], Ashley L. Kiemen[5], Benoit G. Bruneau[2,6,7,8,#]

[#]corresponding authors

[1] Department of Anesthesia and Perioperative Care, University of California, San Francisco, San Francisco, CA

[2] Gladstone Institutes, San Francisco, CA

[3] Department of Medicine, University of California, San Francisco, San Francisco, CA

[4] Department of Pathology, University of California, San Francisco, San Francisco, CA

[5] Department of Chemical and Biomolecular Engineering, Johns Hopkins University, Baltimore, MD

[6] Roddenberry Center for Stem Cell Biology and Medicine, Gladstone Institutes, San Francisco, CA

[7] Cardiovascular Research Institute, University of California, San Francisco, San Francisco, CA

[8] Department of Pediatrics, University of California, San Francisco, San Francisco, CA

Abstract. (147 words).

Failure of septation of the interventricular septum (IVS) is the most common congenital heart defect (CHD), but mechanisms for patterning the IVS are largely unknown. We show that a *Tbx5*$^{+}$/*Mef2cAHF*$^{+}$ progenitor lineage forms a compartment boundary bisecting the IVS. This coordinated population originates at a first- and second heart field interface, subsequently forming

a morphogenetic nexus. Ablation of *Tbx5*$^{+}$/*Mef2cAHF*$^{+}$ progenitors cause IVS disorganization, right ventricular hypoplasia, and mixing of IVS lineages. Reduced dosage of the CHD transcription factor TBX5 disrupts boundary position and integrity, resulting in ventricular septation defects (VSDs) and patterning defects including *Slit2* and *Ntn1* misexpression. Reducing NTN1 dosage partly rescues cardiac defects in *Tbx5* mutant embryos. Loss of *Slit2* or *Ntn1* causes VSDs and perturbed septal lineage distributions. Thus, we identify essential cues that direct progenitors to pattern a compartment boundary for proper cardiac septation, revealing new mechanisms for cardiac birth defects.

Main.

Alterations to the orchestrated patterning of heart development can lead to CHDs. CHDs are the most common birth defects and are a leading non-infectious cause of death in the first year of life. Nearly half of patients with CHDs have ventricular septal defects (VSDs) or atrial septal defects (ASDs), in isolation or in combination with other anatomic defects, including abnormal chamber formation. For example, atrioventricular canal (AVC) defects include VSDs, ASDs and abnormal development of the atrioventricular (AV) valves, with severe cases leading to chamber hypoplasia and functional single ventricle physiology. There is a large gap in our understanding of how early developmental events pattern cardiac morphogenesis and anatomy. Addressing this understudied need can inform diagnostic prognosis, family planning and therapeutic approaches for CHDs.

Complete atrioventricular septation into four chambers allows for separation of systemic and pulmonary circulations and enables higher levels of oxygen for transport in arterial blood. Some progress has been made to determine the embryology of the primordium for the ventricular septum.[1,23] A dye-labelled approach in chick embryos revealed that labelling of the ventral surface of the linear heart tube becomes positioned at the outer curvature of the linear heart tube [1,2]. When labelled at the outer curvature upon rightward looping, the label was found at the apical

53 border of the primary interventricular foramen [1,2]. Discovery of the *Ganglion Nodosum* epitope
54 from chick, which demarcated the primary interventricular foramen and subsequently the IVS, AV
55 junction and ventricular conduction system in mouse, chick and humans, led to the description of
56 a "primary ring" for the ventricular septum [3–5].

57 Discrete early cardiac progenitors in mesoderm contribute to specific cardiac anatomy [6–
58 8]. The first heart field (FHF) gives rise primarily to the left ventricle (LV) and parts of the atria,
59 while the second heart field (SHF) contributes predominantly to the right ventricle (RV), outflow
60 tract (OFT) and portions of the atria [9]. The heart fields can be largely recapitulated by marking
61 lineage-labelled progenitors at gastrulation. Specifically, a lineage labelled by the CHD-linked
62 transcription factor *Tbx5* (*Tbx5*$^+$-lineage) contributes to the LV and atria, while the anterior heart
63 field enhancer of *Mef2c* (*Mef2cAHF*$^+$)-lineage largely contributes to the RV and OFT [6].

64 Both the LV and RV lineages supply descendants to the interventricular septum (IVS) and
65 establish a mutual border between the two lineages [6,10]. Clonal analysis shows segregation at the
66 IVS of the two lineages into non-intermingling cellular compartments, on either the left or right
67 sides of the IVS [6,10]. This lineage configuration is reminiscent of a compartment boundary in
68 *Drosophila* wing imaginal disc or at the vertebrate midbrain-hindbrain boundary [11–13]. Using an
69 intersectional-lineage labelling approach, a subset of cardiac progenitor cells labeled by both
70 *Tbx5*$^+$*/Mef2cAHF*$^+$ were described with contributions to the left side of this apparent compartment
71 boundary [6]. Understanding the role of the *Tbx5*$^+$*/Mef2cAHF*$^+$ lineage-labeled compartment
72 boundary at the IVS may reveal clues about IVS patterning with potential relevance for VSD
73 etiologies. More broadly, how disturbances to compartment boundaries contribute to birth defects
74 is largely unknown.

75 Here, we combined genetic lineage labeling with light sheet microscopy to follow
76 contributions of *Tbx5*$^+$*/Mef2cAHF*$^+$ precursors to a compartment boundary during cardiac
77 morphogenesis. We ablated *Tbx5*$^+$*/Mef2cAHF*$^+$ precursors to determine the essential roles of the
78 lineage-labeled compartment boundary for cardiac septation and chamber development. We

79 leveraged a genetic lesion of the CHD gene *Tbx5* to uncover the genetic regulation of the
80 *Tbx5*$^{+}$*/Mef2cAHF*$^{+}$ lineage-labeled compartment boundary for proper IVS formation. We deployed
81 single cell RNA sequencing (scRNAseq) to discover novel Tbx5-sensitive cues that are essential
82 for compartment boundary regulation of IVS patterning during heart development.
83
84 Results.
85 Early cardiac progenitors for the IVS, IAS and AVC. We used conditional dual lineage labelling
86 by *Tbx5*$^{CreERT2/+}$ or *Mef2cAHF-DreERT2* and marked cells during gastrulation at embryonic day
87 (E)6.5 by tamoxifen-induced recombination. We followed reporter-labeled lineages by
88 epifluorescence microscopy, histology or light sheet microscopy (Figure 1). At E14.5, the *Tbx5*$^{+}$
89 lineage contributed to the left side of the IVS, often ending at a presumptive line marked at the
90 apex by the IV groove, consistent with previous reports suggesting a lineage boundary [6,10]. *Tbx5*$^{+}$
91 and *Mef2cAHF*$^{+}$ lineages showed largely complementary patterns, with notable overlap of *Tbx5*$^{+}$
92 and *Mef2cAHF*$^{+}$ lineages at the IVS, AVC and IAS (Figure 1B, D, F). To better visualize the
93 *Tbx5*$^{+}$*/Mef2cAHF*$^{+}$ lineage, we used a conditional intersectional-lineage labeling approach. Using
94 lineage reporters responsive to both CreERT2 and DreERT2 [14], we observed a striking spatial
95 pattern of the *Tbx5*$^{+}$*/Mef2cAHF*$^{+}$ lineage in the IVS, AVC and IAS. At E14.5, the septal lineage
96 extended to the apex of the heart via the IVS, to the base of the heart at the AV canal, as well as
97 to the IAS superiorly[15–18] (Figure 1H-J). These results expanded upon previous findings in the
98 developing IVS at E10.5 [6], by identifying contributions from *Tbx5*$^{+}$*/Mef2cAHF*$^{+}$ progenitors to
99 additional anatomic sites during chamber formation and septation. Moreover, we deduced that
100 lineage contributions to sites of cardiac septation were derived from *Tbx5*$^{+}$*/Mef2cAHF*$^{+}$ progenitors
101 at E6.5 (Supp. Figure 1), but not later at E8.5 or E10.5, implicating a narrow, early window for
102 capturing *Tbx5*$^{+}$*/Mef2cAHF*$^{+}$ septal progenitors during cardiac mesoderm formation.
103

104 *Tbx5*$^{+}$*/Mef2cAHF*$^{+}$ septal lineage is prefigured in early mouse heart development. To assess the
105 lineage derived from *Tbx5*$^{+}$*/Mef2cAHF*$^{+}$-septal progenitors during early heart development, we
106 examined the localization of the lineage prior to heart tube formation at E8.0 (Figure 2). By light
107 sheet imaging, the pattern of the *Tbx5*$^{+}$*/Mef2cAHF*$^{+}$ lineage was detected at the dorsal aspect of
108 the *Tbx5*$^{+}$ lineage, at an interface between the presumptive first and second heart fields (Figure
109 2A-E"). Cell segmentation at this early stage revealed that the *Tbx5*$^{+}$*/Mef2cAHF*$^{+}$ lineage
110 resembled a nascent halo of cells that became readily apparent at later stages of heart
111 development (Figure 2F-I).

112 We further examined the lineage contributions of *Tbx5*$^{+}$*/Mef2cAHF*$^{+}$ septal progenitors at
113 subsequent timepoints during cardiac morphogenesis. By light sheet microscopy at the linear
114 heart tube stage at E8.25, the labeled *Tbx5*$^{+}$*/Mef2cAHF*$^{+}$ lineage appeared intricately arranged
115 into a ring of cells between the future left and right ventricles (Figure 2J, K). This circlet
116 configuration was maintained during rightward looping of the heart at E8.5 (Figure 2O-Q) and
117 subsequent chamber formation. At E10.5, we observed a band of lineage-labeled cells from the
118 interventricular groove at the outer curvature to the inner curvature near the AV groove that
119 extended posteriorly to the atria (Figure 2R-T), reminiscent of the "primary ring" [3–5]. Optical
120 sections showed the labeled lineage superiorly at a crossroads of the AVC, outflow tract and atria
121 (Figure 2S). This populates a morphogenetic nexus where VSDs can occur due to abnormal
122 connections between the IVS and the AV cushions, outflow tract cushions, or the muscular
123 septum itself. In the atria, we noted lineage-labeled cells at the midline, superiorly and inferiorly,
124 suggesting that the Tbx5^{+}/Mef2cAHF^{+} lineage potentially mark the presumptive location of the
125 IAS for later stages (Supp. Figure 2B-E). Consequently, this data is consistent with a notion that
126 the *Tbx5*$^{+}$*/Mef2cAHF*$^{+}$ lineage is configured early in heart development, well before subsequent
127 morphogenetic events such as chamber formation and cardiac septation.
128

129 IVS disorganization and ventricular hypoplasia from cell ablation of Tbx5^{+}/Mef2cAHF^{+}
130 progenitors. To determine a role for the *Tbx5^{+}/Mef2cAHF^{+}* septal progenitors, we conditionally
131 ablated these cells at E6.5, then evaluated heart development. We generated an intersectional
132 recombinase-responsive *DTA176* transgenic mouse line at the *Hip11* safe harbor locus, by which
133 cells would be killed where approximately 100-200 molecules of DTA176 were expressed [15]. Upon
134 tamoxifen administration to pregnant dams at E6.5, intersectional-*DTA* mutant (*Tbx5$^{CreERT2/+}$;*
135 *Mef2cAHF-DreERT2; Hip11$^{Intersectional\text{-}DTA176/+}$*) embryos at E9.5 displayed RV hypoplasia (Figure
136 3A, B). At E12.5, RV hypoplasia persisted (Figure 3C-J), and the IVS was disorganized and non-
137 compacted at a blunted IV groove (Figure 3H, J). Further, there were defects of the AV cushions
138 and absence of the IAS (Figure 3H, J). A few *Tbx5^{+}/Mef2cAHF^{+}* lineage cells remained in mutant
139 embryos, likely reflecting some degree of inefficient dual recombination of both the reporter allele
140 and the intersectional-*DTA* transgene. Beyond E12.5, intersectional-*DTA* mutant embryos were
141 not recovered. Hence, these findings suggested that the *Tbx5^{+}/Mef2cAHF^{+}* septal progenitors
142 were not only important for IVS development and AV septation, but also for RV chamber
143 formation.
144
145 Lineage mixing from disruption of an IVS compartment boundary upon ablation of
146 *Tbx5^{+}/Mef2cAHF^{+}* septal progenitors. We hypothesized that the *Tbx5^{+}/Mef2cAHF^{+}* septal
147 progenitors establish a compartment boundary at the IVS. Upon ablation of *Tbx5^{+}/Mef2cAHF^{+}*
148 septal progenitors, we predicted that if either lineage expanded into the other ventricular chamber,
149 then this would suggest lineage mixing from loss of compartment boundary integrity. To determine
150 if *Tbx5^{+}/Mef2cAHF^{+}* septal progenitors were essential for a compartment boundary at the IVS, we
151 tested the effects of ablating *Tbx5^{+}/Mef2cAHF^{+}* septal progenitors on lineage segregation. We
152 quantified the distributions of the *Mef2cAHF^{+}* or *Tbx5^{+}* lineages at E10.5 after tamoxifen
153 administration at E6.5, by quantifying fluorescence intensity as a linear profile across the
154 ventricular chambers by light sheet microscopy. In control (*Tbx5$^{CreERT2/+}$;Mef2cAHF-*

155 *DreERT2;Hip11*$^{+/+}$) (n=2) embryos at E10.5, cells of the *Mef2cAHF*$^{+}$ lineage were enriched in the
156 RV. Cells of the *Tbx5*$^{+}$ lineage were highly enriched in the LV and rarely found in the RV, and
157 both lineages overlapped at the developing IVS. This data was consistent with observations of
158 lineage segregation at the IVS during later stages of heart development. However, in mutant
159 intersectional-*DTA* (*Tbx5*$^{CreERT2/+}$*;Mef2cAHF-DreERT2;Hip11*$^{Intersectional\text{-}DTA176/+}$) (n=2) embryos at
160 E10.5, cells of the *Mef2cAHF*$^{+}$ lineage were less leftward in the corresponding region of targeted
161 cell ablation, suggesting a rightward retreat of the Mef2cAHF^{+} lineage from ablation of
162 *Tbx5*$^{+}$*/Mef2cAHF*$^{+}$ progenitors. In contrast, cells of the Tbx5^{+} lineage in intersectional-*DTA*
163 mutants were observed more rightward, including in the RV. Therefore, we inferred that
164 *Tbx5*$^{+}$*/Mef2cAHF*$^{+}$ progenitors were essential for preventing lineage mixing between the RV and
165 LV, by maintaining compartment boundary integrity at the developing IVS.
166
167 <u>Heterozygous loss of *Tbx5* in the IVS leads to VSDs</u>. *TBX5* is a transcription factor gene that
168 causes VSDs in Holt-Oram Syndrome from haploinsufficiency in humans [16–18] and mice [19]. We
169 wondered if heterozygous loss of *Tbx5* in the IVS alone would cause VSDs. We used the
170 *Mef2cAHF-Cre* [20] in combination with a conditional deletion of *Tbx5* (*Tbx5*^{flox}) [19], to conditionally
171 delete *Tbx5* heterozygously in a domain that overlaps with *Tbx5* expression at the IVS [21]. We
172 observed membranous VSDs in *Mef2cAHF-Cre*;*ROSA26*$^{mTmG/+}$*;Tbx5*$^{flox/+}$ mutant embryos (n=4/7)
173 compared to controls (n=0/3), at E14.5 (Supp. Figure 3A-C). This result contrasted with a previous
174 report that did not identify VSDs, albeit using a mixed genetic background [22]. This provided
175 evidence that appropriate *Tbx5* dosage in the IVS was essential for proper ventricular septation.
176
177 <u>Disturbed septal lineage contributions from reduced *Tbx5*.</u> As TBX5 dosage reduction globally or
178 only in the IVS results in VSDs, we reasoned that reducing TBX5 dosage may affect the regulation
179 of the *Tbx5*$^{+}$*/Mef2cAHF*$^{+}$ septal progenitors and their subsequent lineage contributions. We
180 evaluated a reduction of *Tbx5* using a hypomorphic (*Tbx5*^{CreERT2}) allele [18] in combination with a

181 conditional deletion of *Tbx5* (*Tbx5*^{flox}) [19] at E6.5. This resulted in levels of *Tbx5* that are estimated
182 to be about 25% of wildtype in the *Tbx5*$^{+}$ lineage. In control (*Tbx5*$^{CreERT2/+}$*;Mef2cAHF-*
183 *DreERT2;Rosa26*$^{Ai66/Ai6}$) embryos, the *Tbx5*$^{+}$*/Mef2cAHF*$^{+}$ septal lineage overlapped at the lineage
184 front of the *Tbx5*$^{+}$ lineage in the IVS, from the base to the apex of the heart at the IV groove,
185 spanning from anterior to posterior of the heart in the IVS (Figure 4A-A", Supp. Figure 4A, B).
186 Among *Tbx5*$^{CreERT2/flox}$ mutant (*Tbx5*$^{CreERT2/flox}$*;Mef2cAHF-DreERT2;Rosa26*$^{Ai66/Ai6}$) embryos, we
187 found that reduced TBX5 dosage at E6.5 caused a spectrum of defects, frequently including
188 VSDs, ASDs and AVC defects at E14.5 (Figure 4B-D'), reminiscent of features of Holt-Oram
189 Syndrome [16,17,23]. The normally organized distribution of the tdTomato^{+} cells was highly irregular
190 in the *Tbx5*$^{CreERT2/flox}$ mutant hearts regardless of VSDs (Supp. Figure 4A-H). Often, tdTomato^{+}
191 cells were less apparent in the posterior IVS (Figure 4A', A", B', B", C', C", D'), and tdTomato^{+}
192 cells were nearly absent in a heart that displayed a severe AVC defect and chamber hypoplasia
193 (Figure 4D, D', Supp Figure 4G, H).

194 We used quantitative morphometry to assess the position and distribution of the
195 *Tbx5*$^{+}$*/Mef2cAHF*$^{+}$ septal lineage at the IVS. We tested this by quantifying linear profiles of the
196 labeled *Tbx5*$^{+}$*/Mef2cAHF*$^{+}$ septal lineage in the heart. We found that both distribution and position
197 of the *Tbx5*$^{+}$*/Mef2cAHF*$^{+}$ septal lineage was disturbed in *Tbx5*$^{CreERT2/flox}$ mutant (n=3; control,
198 n=4)(Figure 4E-H, Supp. Figure 4I, J), including an increase of tdTomato^{+} cells leftward in the LV,
199 suggesting abnormal lineage position. As well, we observed a broader band of *Tbx5*$^{+}$*/Mef2cAHF*$^{+}$
200 septal lineage cells, suggesting that proper TBX5 dosage maintains integrity of the compartment
201 boundary marked by the *Tbx5*$^{+}$*/Mef2cAHF*$^{+}$ lineage at the IVS (Figure 4G, H). We also observed
202 a reduction, or sometimes absence, of the labeled septal lineage in AVC cells, as well as remnant
203 atrial septal tissue in *Tbx5*$^{CreERT2/flox}$ mutants (Figure 4D, D').

204 We further observed that cells of the *Tbx5*$^{+}$*/Mef2cAHF*$^{+}$ lineage in the IVS were arranged
205 like a stack of coins, especially from the apex to the mid-septum (Figure 4A"). We wondered if
206 proper TBX5 dosage might be necessary for maintaining appropriate cell orientation in the IVS.

207 Therefore, cell alignment was determined and quantified by two metrics, average orientation
208 score or directional coherency. In *Tbx5*$^{CreERT2/flox}$ mutant hearts, *Tbx5*$^{+}$/*Mef2cAHF*$^{+}$ lineage
209 (tdTomato^{+}) and *Tbx5*$^{+}$ lineage (ZsGreen^{+}) cells were reduced in the dominant direction of cell
210 orientation and were more frequently in the orientation orthogonal to the dominant direction
211 (Figure 4S, Supp. Figure 4T). Further, both lineages demonstrated worse directional coherency
212 in *Tbx5*$^{CreERT2/flox}$ mutants (Figure 4T, Supp. Figure 4U), implicating TBX5 in proper cell orientation
213 in the IVS.
214
215 <u>*Tbx5*-sensitive genes encode guidance cues</u>. To find downstream effectors of Tbx5 that may
216 mediate the regulation of *Tbx5*$^{+}$/*Mef2cAHF*$^{+}$ lineage cells, we applied single cell RNA sequencing
217 at E13.5, prior to completion of ventricular septation. We micro-dissected the RV, LV and
218 IVS+AVC in controls (*Tbx5*$^{CreERT2/+}$*;Mef2cAHF-DreERT2;Rosa26*$^{Ai66/Ai6}$) (n=4) and *Tbx5* mutants
219 (*Tbx5*$^{CreERT2/flox}$*;Mef2cAHF-DreERT2;Rosa26*$^{Ai66/Ai6}$) (n=2) (Figure 5A). These samples were
220 labeled at E6.5 for progenitors of the *Tbx5*$^{+}$/*Mef2cAHF*$^{+}$ lineage (*tdTomato*$^{+}$) and *Tbx5*$^{+}$ lineage
221 (*ZsGreen*$^{+}$). In samples from each cardiac tissue region, we detected clusters enriched for *Tnnt2*$^{+}$
222 cardiomyocytes (CMs), *Postn*$^{+}$ fibroblasts, *Plvap*$^{+}$ endothelial cells, *Tbx18*$^{+}$/*Wt1*$^{+}$ epicardial cells,
223 *Hbb-b2*$^{+}$ red blood cells, and *C1qb*$^{+}$ white blood cells (Figure 5B, Supp. Figure 5A-F).
224 In particular, *tdTomato*$^{+}$ cells were most abundant among clusters of *Tnnt2*$^{+}$
225 cardiomyocytes (CMs) of the IVS+AVC region (Figure 5C). However, we were unable to identify
226 a gene expression signature that was unique to the *Tbx5*$^{+}$/*Mef2cAHF*$^{+}$ lineage, beyond the lineage
227 marker itself, at this stage. Likewise, *ZsGreen*$^{+}$ cells were also enriched among clusters of *Tnnt2*$^{+}$
228 CMs in this region (Figure 5D), indicative of the *Tbx5*$^{+}$ lineage contribution to CMs in the region,
229 as well as a site of conditional reduction of *Tbx5* among *Tbx5* mutants.
230 We then focused our analysis on a subset of *Tnnt2*$^{+}$ enriched clusters from IVS+AV canal
231 regions. We identified genotype-enriched clusters that were abundant with cells from controls
232 (Cluster 5) or *Tbx5* mutants (Cluster 10) (Figure 5E, F). Control-enriched cluster 5 included genes

233 expressed in the AV canal region, encoding the Wnt co-receptor *Rspo3*, morphogen *Bmp2*, and
234 transcription factors *Tbx2* and *Tbx3*, suggesting that these genes are reduced in *Tbx5* mutants
235 (Figure 5G, H). As well, the SLIT-receptor *Robo1,* which is implicated in mouse and human VSDs
236 [24–26], and Netrin-receptor *Unc5b,* were also downregulated in *Tbx5* mutant cells (Figure 5G, H).
237 In the mutant-enriched cluster 10, genes typically expressed in ventricular trabeculae were
238 enriched (Figure 5G, H). These included natriuretic peptide *Nppa*, transcription factor *Cited1,* and
239 bone morphogenetic protein *Bmp10*, suggesting ectopic expression of these trabecular genes in
240 the IVS of *Tbx5* mutants. Intriguingly, guidance cues *Netrin1* (*Ntn1)* and *Slit2,* which are best
241 known for axonal development or vasculogenesis [27], were also dysregulated (Figure 5G, H).
242 We examined differential gene expression between controls or *Tbx5* mutants in *tdTomato*$^+$
243 (Tbx5$^+$/Mef2cAHF$^+$ septal lineage) or *ZsGreen*$^+$ (Tbx5$^+$ lineage) CMs. We found many
244 differentially expressed genes that overlapped among comparisons of *tdTomato*$^+$ or *ZsGreen*$^+$
245 clusters, including *Nppa*, *Cited1,* and *Slit2*, consistent with findings from cluster-to-cluster
246 comparisons (Supp. Figure 5G, H).
247 We used orthogonal assays to validate candidate TBX5-sensitive genes. By fluorescence
248 *in situ* hybridization in formalin fixed paraffin embedded (FFPE) sections, we observed a reduction
249 of gene expression of *Bmp2, Robo1 and Unc5b* in the AV canal region of mutant hearts when
250 compared to controls. (Supp. Figure S6M-X'). As well, we detected expansion of gene expression
251 of *Nppa* and *Slit2* in the IVS and compact layer of mutant hearts, both of which are normally
252 expressed only in the trabecular regions of both ventricles of control hearts (Figure 5I-L').
253 Moreover, we discovered *Ntn1* expression enriched in LV trabeculae and in a gradient across the
254 control IVS (Figure 5M, M'), consistent with immunostaining of NTN1 in the heart at E14.5 (Supp.
255 Figure 6Y). Notably, *Ntn1* was enriched in the LV earlier at E11.5 during ventricular septation
256 (Supp. Figure 6Z). However, in *Tbx5* mutants, the *Ntn1* gradient was flattened and expanded in
257 the IVS by reduced Tbx5 dosage (Figure 5N, N'). Interestingly, we observed changes of *Nppa*,
258 *Slit2* and *Ntn1* in *Tbx5* mutants with or without VSDs, suggesting that this dysregulated gene

259 expression was not secondary to VSDs (Supp Figure 6A-L'). In addition, analysis of ChIP-seq of
260 TBX5 from embryonic mouse hearts [28] showed TBX5 occupancy at promoters of *Nppa, Slit2*, and
261 *Ntn1* (Supp Figure 7A-C), suggesting these guidance genes are likely to be direct targets of TBX5
262 in the heart.
263
264 *Tbx5-Slit2* and *Tbx5-Ntn1* genetic interactions. We evaluated if genetic interactions existed
265 between *Tbx5* and *Slit2* or *Ntn1*. As *Tbx5* heterozygous mutant (*Tbx5*$^{del/+}$)[19] mouse embryos
266 display muscular or membranous VSDs, we wondered if heterozygous *Slit2* or *Ntn1* loss of
267 function (LOF) mutant embryos might alter *Tbx5*-dependent phenotypes. We mated *Tbx5*$^{del/+}$ mice
268 with either *Slit2* (*Slit2*$^{+/-}$) or *Ntn1* (*Ntn1*$^{beta\text{-}actin\text{-}Cre/+}$ referred here subsequently as *Ntn1*$^{+/-}$[29,30])
269 heterozygous LOF mice. In *Tbx5*$^{del/+}$ embryos at E14.5, we observed membranous (n=5/8) or
270 muscular (n=3/8) VSDs by histology (Supp. Figure 8B, E), consistent with previous reports [19].
271 Among *Slit2*$^{+/-}$ embryos at E14.5, we observed a membranous VSD (n=1/8) (Supp. Figure 8C, E).
272 This contrasted with a previous report that did not detect any VSDs in *Slit2*$^{+/-}$ albeit using a
273 different mutant *Slit2* allele [24]. In *Tbx5*$^{del/+}$;*Slit2*$^{+/-}$ compound heterozygous embryos, we observed
274 an estimated decrease in the incidence of membranous VSDs (n=5/8) (Supp. Figure 8D, E), which
275 approached significance (log OR -2.5; $p<0.09$ in a Generalized Linear Model).
276 We next tested if there was a genetic interaction between *Tbx5* and *Ntn1* (Supp. Figure
277 8F-J). In *Ntn1*$^{+/-}$embryos, we observed a membranous (n=1/9) or a muscular (n=1/9) VSD. In
278 *Tbx5*$^{del/+}$;*Ntn1*$^{+/-}$ compound heterozygous embryos, we observed a significant decrease of
279 membranous VSDs (n=1/8; log OR -5.3; $p<1x10^{-3}$ by a Generalized Linear Model), but not
280 significant changes to prevalence of muscular VSDs (n=4/8; log OR 0.12; $p<0.93$), consistent with
281 a genetic interaction between *Tbx5* and *Ntn1* for ventricular septation.
282 We wondered if there were other quantitative histologic differences, in addition to the
283 changes in incidence of VSD types. To quantify morphometry from histology, we leveraged a
284 deep learning algorithm, known a CODA [31], to detect embryonic mouse heart components from

285 hematoxylin and eosin (H&E) sections. We generated three-dimensional (3-D) tissue
286 reconstructions, to visualize and quantify anatomic structures and CHDs, including membranous
287 and muscular VSDs, at cellular resolution (Figure 6I-K). Using this machine learning method, we
288 discovered that the cell density of the IVS, which we termed IVS fill, was increased in *Tbx5*$^{del/+}$;
289 *Ntn1*$^{+/-}$ embryos compared to wildtype ($p<0.05$ by Fisher's exact test), while classification of the
290 IVS as trabecular was significantly reduced in *Tbx5*$^{del/+}$;*Ntn1*$^{+/-}$ embryos ($p<0.05$ by Fisher's exact
291 test) (Supp. Figure 8M). In addition, we estimated the minimal area for each membranous or
292 muscular VSD, when present (Supp. Figure 8O, P). In *Tbx5*$^{del/+}$;*Slit2*$^{+/-}$ compound mutants, we
293 detected statistically significant levocardia ($p<0.001$ by Fisher's exact test), as determined by the
294 axis of the heart compared to the spine and sternum (Supp. Figure 8Q). This uncovered a genetic
295 interaction between *Tbx5* and *Slit2* related to heart position, demonstrating that machine learning-
296 based morphometry can quantify unexpected anatomic findings.
297
298 <u>*Slit2* and *Ntn1* for ventricular septation.</u> To determine if *Slit2* or *Ntn1* are essential for ventricular
299 septation, we evaluated homozygous LOF mouse mutants for *Slit2* or *Ntn1* for VSDs. In *Slit2*$^{-/-}$
300 embryos at E14.5, we observed that homozygous loss of *Slit2* displayed complete penetrance for
301 VSDs, including membranous (n=4/4; log OR 5.0, $p<0.00$) or muscular VSD (n=1/4) (Figure 6A-
302 D), demonstrating a far higher incidence than a previous report using an alternative *Slit2* LOF
303 allele [24]. Further, we detected statistically significant a non-compacted IVS as determined by
304 reduced IVS fill and thinning of the right ventricular compact layer (Supp. Figure 9E, H). Likewise,
305 *Ntn1*$^{-/-}$ embryos displayed membranous VSDs (n=6/7), an apparent thinning of the ventricular
306 compact layer and a non-compacted IVS, although these observations were not statistically
307 significant (Supp. Figure 9). Collectively, this morphologic evidence implicates *Slit2* and *Ntn1* in
308 proper ventricular septation during heart development.
309

310 As *Slit2* and *Ntn1* were necessary for ventricular septation, we asked if loss of *Slit2* or *Ntn1* might
311 disturb distribution of the Tbx5^{+}/Mef2cAHF^{+} lineage in the IVS. In homozygous *Slit2* LOF mutants
312 with the lineage reporter (*Tbx5*$^{CreERT2/+}$;*Mef2cAHF-DreERT2*;*ROSA26*$^{Ai66/+}$;*Slit2*$^{-/-}$) (n=4), we
313 observed a statistically-significant broadened distribution of the Tbx5^{+}/Mef2cAHF^{+} lineage
314 compared to controls (n=2) (Figure 6N-Q), consistent with lineage mixing from boundary
315 disruption and implicating a role for SLIT2 in maintaining boundary integrity. Conversely,
316 homozygous *Ntn1* LOF mutants with the lineage reporter (*Tbx5*$^{CreERT2/+}$;*Mef2cAHF-DreERT2*;
317 *ROSA26*$^{Ai66/+}$;*Ntn1*$^{-/-}$) (n=6) demonstrated leftward displacement of the Tbx5^{+}/Mef2cAHF^{+} lineage
318 compared to controls (n=4) (Figure 6R-U), implying that NTN1 signaling precisely positions the
319 compartment boundary at the IVS. Taken together, this evidence suggested that SLIT2- and
320 NTN1-signaling, as part of a Tbx5-dependent pathway, regulates the position and integrity of the
321 compartment boundary labeled by the Tbx5^{+}/Mef2cAHF^{+} lineage.

322

323 **Discussion.**

324 We show that *Tbx5*$^{+}$/*Mef2cAHF*$^{+}$ progenitors prefigure a compartment boundary that
325 becomes located at the junction between the left and right sides of the IVS, providing a cellular
326 framework during development for heart patterning. Our study underscores a fundamental
327 principle that early developmental events preconfigure structure and function of the heart and are
328 susceptible to genetic risks that cause CHDs.

329 Compartment boundaries have been defined by several criteria. First, a compartment
330 boundary segregates juxtaposed cell populations such as distinct cell lineages to restrict cell
331 intermingling, and ablation of the boundary leads to cell mixing. Second, the expression domain
332 of a selector gene corresponds with a compartment domain, loss of the selector gene eliminates
333 the identity in this territory, and ectopic expression of the selector induces this identity. Third, a
334 selector gene establishes a signaling center to maintain the compartments and boundary. Our
335 results satisfy all of these criteria: Ablation of the *Tbx5*$^{+}$/*Mef2cAHF*$^{+}$ lineage disrupts segregation

336 of *Tbx5*$^{+}$ lineage cells in the LV from the *Tbx5*$^{-}$ lineage in the RV of the developing heart. Reduced
337 *Tbx5* expression impairs the integrity of the boundary and its patterning, and in previous work
338 misexpression of TBX5 eliminates IVS formation [21]. Third, TBX5 patterns signaling molecules that
339 are important for morphologies that impact the boundary. In this context, we postulate that *Tbx5*
340 may function as a candidate selector gene. Further experiments will be needed to formally
341 ascertain this.

342 In this context, we identify a *Tbx5*-dependent pathway that regulates *Slit2* and *Ntn1*.
343 Normally, TBX5 represses their ectopic expression in the IVS and compact layer. Both SLIT2 and
344 NTN1 are guidance or adhesive cues in several developmental contexts. Here, we provide
345 evidence that *Slit2* and *Ntn1* are direct targets of TBX5, and that *Tbx5* and *Slit2* or *Ntn1* genetically
346 interact. Further, we found that *Slit2* and *Ntn1* are essential for proper ventricular septation, as
347 well as compartment boundary integrity and positioning, respectively. Like TBX5, proper
348 ventricular septation may be sensitive to imbalanced dosage of SLIT2 or NTN1. As *Ntn1*
349 expression is enriched in the LV and left-side of the IVS in the *Tbx5*$^{+}$ compartment, we propose
350 a working hypothesis that NTN1 functions as a TBX5-dependent signaling center for compartment
351 boundary regulation.

352 The spatiotemporal position of the boundary is at the crux of cardiac septation and, when
353 disrupted, spans sites for congenital cardiac anomalies. The sensitivity of the *Tbx5*$^{+}$/*Mef2cAHF*$^{+}$
354 lineage-labeled boundary to genetic perturbations, specifically *Tbx5* deficiency, is of significance
355 in the context of congenital heart disease. Such deficiency selectively compromises the
356 boundary's integrity and position, along with disturbances to cell orientation, leading to VSDs or
357 AVSDs. This observation suggests that genetic pathways for patterning, like the
358 *Tbx5*$^{+}$/*Mef2cAHF*$^{+}$ lineage-labeled boundary, can be exceptionally susceptible to genetic
359 disruptions. Whether additional genetic perturbations that cause VSDs or AVSDs disrupt the
360 compartment boundary remains to be determined. Likewise, it will be interesting to evaluate if the
361 *Tbx5*$^{+}$/*Mef2cAHF*$^{+}$ lineage-labeled boundary corresponds with abnormal shifts in IVS position, like

362 those observed in the endothelial loss of *Hand2*, which displays rightward shifted IVS and double
363 inlet left ventricle (DILV) or two IVS primordia [32,33].

364 In conclusion, our research demonstrates the delicate interplay of progenitor cell behavior,
365 gene expression and boundary formation that determines heart development and genetic
366 susceptibility that increases the risk of CHDs. This evidence further underscores the significance
367 of early developmental stages for the ontogeny of some CHDs. The implications of these
368 discoveries likely extend beyond cardiac morphogenesis, as these findings offer insights for the
369 roles of compartment boundaries during mammalian development and uncover a vulnerability for
370 organ patterning from genetic disturbances.

371

372 **METHODS.**

373 **Mouse lines.** All mouse protocols were approved by the Institutional Animal Care and Use
374 Committee at UCSF. Mice were housed in a barrier animal facility with standard husbandry
375 conditions at the Gladstone Institutes. Mice of *Tbx5*^{CreERT2IRES2xFLAG} (abbreviated here as
376 *Tbx5*^{CreERT2}) and *Mef2cAHF-DreERT2* [6], *Tbx5*$^{del/+}$ and *Tbx5*$^{flox/+}$ [19], *ROSA26*^{Ai66} and *ROSA26*^{Ai6} [14]
377 were described previously. *Mef2cAHF-Cre*$^{/+}$ mice [20] were obtained from Brian Black. *Slit2*$^{+/-}$ mice
378 (MMRC, Strain 065588-UCD, donated by Kent Lloyd) were generated by CRISPR/Cas9-
379 targeted constitutive deletion of exon 8 and flanking splicing regions of *Slit2*. *Ntn1*$^{+/-}$ mice
380 were derived from matings of *Ntn1* floxed mice (*Ntn1*$^{flox/+}$; Jackson Laboratory #028038) [34]
381 to beta-actin-Cre [30], which were obtained from Gail Martin. All mouse strains were maintained
382 in the C57BL6/J background (Jackson Laboratory #664), except for *Tbx5*$^{del/+}$, which was
383 maintained in Black Swiss (Charles River, Strain Code 492), and *Slit2*$^{+/-}$ which was maintained in
384 C57BL6/N (Jackson Laboratory, #005304). Both male and female embryos were collected from
385 timed matings and used at random for experiments.

386

387 **Cloning and generation of mouse lines.**

388 We generated an attenuated diptheria toxin (DTA176) transgenic knock-in mouse under the
389 control of the dual-recombinase intersectional cassette. DTA176 encodes an attenuated form of
390 toxic fragment A from diptheria toxin [15], which requires ~100-200 molecules for cell killing. This
391 strategy was an effort to reduce potential problems of leaky DTA expression prior to recombinase-
392 mediated activation. Briefly, DTA176 [15] was cloned downstream of ROX-STOP-ROX and LOX-
393 STOP-LOX sites to create a Dre- and Cre-dependent expression construct, which was derived
394 from the Dre- and Cre-dependent tdTomato expression cassette of the Ai66 (RCRL-tdT) targeting
395 vector [14]. After the tdTomato cassette was removed using MluI sites and replaced by DTA176,
396 the construct was cloned into the TARGATT targeting construct pBT346.3 (Applied Stem Cells)
397 to target the transcriptionally inactive *Hip11* locus [35] using PacI and SmaI restriction enzyme sites.
398 The final construct was verified using restriction digestion and Sanger sequencing. DNA was
399 purified and injected along with mRNA for the Phi31o transposase according to manufacturer's
400 protocol to generate intersectional-DTA mutant (*Hip11*$^{Rox\text{-}STOP\text{-}Rox\text{-}Lox\text{-}STOP\text{-}Lox\text{-}DTA176}$) mice. To
401 generate Ai66b mice (*ROSA26*^{Ai66b}), which is a Dre-dependent tdTomato reporter, the LOX-
402 STOP-LOX sites were removed from the Ai66 (RCRL-tdT) targeting vector [14], and then the
403 transgene cassette was inserted into endogenous genomic loci via homologous recombination,
404 as previously described [36].
405
406 Whole mount embryo and heart immunofluoresence labeling
407 Embryos were dissected from timed pregnant dams, including removal of yolk sac with
408 genotyping, as previously described [6]. Embryos up to E10.5 were fixed for 4 hours with 4% PFA
409 at room temperature, then incubated with gentle rocking in clearing solution (8% SDS in 0.2M
410 borate buffer) at 37°C for 1-3 hours until clear. E13.5 or E14.5 hearts were micro-dissected from
411 freshly harvested embryos in PBS with heparin (10 Units/mL) (Sigma #H3393) or incubated in 1X
412 RBC lysis solution (Roche #11814389001) for 10 minutes at room temperature, fixed at room
413 temperature in 4% PFA for one hour, and incubated with gentle rocking in clearing solution at

414 37°C for 2-4 days until clear. Specimens were permeabilized and blocked for two hours to
415 overnight with gentle rocking at 37°C in blocking buffer (PBS containing 5% normal donkey serum
416 and 0.8% to 1.5% Triton X-100, dependent on embryo/heart stage). Specimens were labeled with
417 primary antibody (list below) in blocking buffer with gentle rocking at 37°C, overnight for embryos
418 up to E10.5, or 5 days for E13.5 or E14.5 hearts with fresh antibody replaced mid-way. Following
419 three washes in blocking buffer, each 45 minutes except the third overnight for E13.5 and E14.5
420 hearts, specimens were labeled with secondary antibody (raised in donkey; AF488-, Dy405-, Cy3,
421 or AF647-conjugated; used at 1:750; Jackson ImmunoResearch) and DAPI in blocking buffer with
422 gentle rocking at 37°C, 2-3 hours for embryos up to E10.5, or 5 days for E13.5 or E14.5 hearts.
423 Following three washes in PBS with gentle rocking at 37°C, samples were stored (up to overnight)
424 in PBS with 0.2% sodium azide. Primary antibodies used were: tdTomato (rabbit, Rockland 600-
425 401-379, 1:1000), MEF2c (R&D AF6786, sheep, 1:250), TNNT2 (mouse, Thermo MS-295-P,
426 1:500). Strong ZsGreen fluorescence persisted after clearing and did not require immunolabeling.
427

428 Lightsheet Image Acquisition

429 Images were acquired by lightsheet microscopy, as described previously [37]. Brielfy, specimens
430 were warmed and transferred to 2% low melting point agarose (Fisher BP165-25) in PBS at 37°C,
431 then embedded in glass capillary tubes with paired pistons (Sigma Z328510 paired with
432 BR701938, or Sigma Z328502 paired with BR701934) for embryos, or tip-truncated 1mL syringes
433 (Becton Dickinson) for hearts. After the gel solidified, the capillaries or syringes were suspended
434 specimen-down from 14mL polystyrene tubes sealed with Parafilm. Columns containing the
435 specimen were partially extended into an ample volume optical clearing solution (OCS, EasyIndex
436 EI-Z1001, LifeCanvas). Following overnight incubation in OCS, specimen capillaries were
437 retracted and were brought to a Light Sheet Z.1 microscope coupled with ZEN software (Carl
438 Zeiss Imaging). With immersion in OCS, specimens were rotated and imaged from multi-view
439 whole-volume approach, to improve fluorescence signal intensity and resolution captured

440 throughout the entire heart volume. One of two objective setups was used: EC Plan Neofluar
441 5X/0.16 with 5X/0.1 pair (hearts), or Clr Plan Neofluar 20X/1.0 paired with 10X/0.2 clearing pair
442 (embryos). Z-stacks were collected at each view angle at the optimal slice thickness
443 determined by Zeiss' Zen software, ranging from 1.42 to 4.95 µm.
444
445 Image Dataset Preprocessing
446 Imaging data was processed, as previously described [37]. All data processing was performed on
447 an 8-core x86-64 desktop PC with 64GB RAM, running Kubuntu 20.04 LTS, principally using Fiji
448 software [38]. Acquired light sheet image stacks were subjected to single-view deconvolution using
449 regularized generalized Tikhonov filtering (Parallel Spectral Deconvolution,
450 https://imagej.net/plugins/parallel-spectral-deconvolution) following theoretical PSF calculation
451 using the intersection of Gaussian z-plane illumination with Gibson-Lanni widefield
452 epifluorescence detection patterns [39]. Deconvolved stacks were co-registered, and image
453 volumes were generated for each desired orientation, for each specimen, using Content Based
454 Fusion in BigStitcher [40]. TrackMate [41] and ImageJ 3-D viewer were leveraged for segmentation
455 and visualization of fused volumes. Macros for the batch automation of these steps are available
456 upon request.
457
458 Image Volume Quantification
459 Extensive whole-volume quantifications of imaged E14.5 hearts were performed using Fiji and
460 associated plugins, with analysis conducted with R statistics. For assessing the location of
461 fluorescence signal, volumes were downsampled, and 2-dimensional regions of interest (ROIs)
462 corresponding to anatomic structures were manually drawn on each Z-slice, using the DAPI
463 channel. Integrated intensity for each fluorescence channel was programatically measured for
464 each ROI, and counts were normalized to DAPI signal and pooled by anatomic region. For whole-

465 heart quantifications, counts were further normalized to combined Ai6 plus Ai66 signal, then and
466 averaged across each anatomic region. For orientation assessments, a multi-channel panel of
467 174 full resolution four-chamber image excerpts were blinded, selected and evenly distributed
468 between apical posterior, apical anterior, posterior basal, and posterior apical IVS, split by channel
469 (tdTomato or ZsGreen) and sampled. Using automated batch processing, samples were
470 subjected to background filtering, contrast enhancement, and measurements of orientation
471 distribution and dominant direction (OrientationJ plugin, https://github.com/Biomedical-Imaging-
472 Group/OrientationJ), and of directionality (Directionality plugin,
473 https://github.com/fiji/Directionality). Orientation score distributions were rotated so that dominant
474 direction was at 0°, and average score (across the panel of images) was plotted as a function of
475 direction and examined by Watson's two-sample test. Individual scores surrounding 0° and 90°
476 were pooled and compared with the Wilcoxon signed-rank test. Directionality coherence scores
477 (across the panel of images) were plotted by genotype and compared with the Wilcoxon signed-
478 rank test. Macros for the batch automation of these steps are available upon request.

479

480 **Quantification of right-left position of lineages.**

481 For each E10.5 heart analyzed, five representative coronal optical sections were selected,
482 approximately 20-35 μm apart. For each optical section, the DAPI channel was used to draw five
483 linear profiles spanning the ventricular chambers from right to left. Linear profiles were drawn
484 such that the "0" position corresponded to the midline, identified by the interventricular groove.
485 Fluorescence intensity of each channel (green=*Tbx5*$^{+}$ lineage, magenta=*Mef2cAHF*+ lineage)
486 was measured along each linear profile, and intensity values were normalized to the maximum
487 value along each profile. Profiles for each channel were grouped by experimental condition (WT
488 or DTA), and then the average ± SEM normalized fluorescence intensity profiles were calculated
489 and plotted. Welch's two-sample t-test was used at each position along the right-left axis to

490 determine regions of significant difference in fluorescence intensity of each channel between
491 experimental groups, indicating a change in the distribution of cells of that lineage.

492 For each E13.5-E14.0 heart analyzed, maximum z-projections were generated from
493 optical sections spanning every 50 μm from the anterior to posterior of the heart. For each
494 maximum z-projection, the DAPI and red or magenta (*Tbx5*$^{+}$/*Mef2cAHF*$^{+}$ intersectional lineage)
495 channels were split and background subtraction was performed on the red or magenta channel
496 using a 50-pixel rolling ball radius. The DAPI channel was used to draw three linear profiles (basal,
497 middle, apical) spanning the ventricular chambers from right to left. Linear profiles were drawn
498 such that the "0" position corresponded to the middle of the IVS. Fluorescence intensity of the red
499 or magenta channel was measured along each linear profile, and intensity values were
500 normalized to the maximum value along each profile. Profiles were grouped by experimental
501 condition (*Tbx5*$^{CreERT2/+}$ or *Tbx5*$^{CreERT2/flox}$) or (e.g. WT, *Ntn1*$^{+/-}$, *Ntn1*$^{-/-}$) and then the average ± SEM
502 normalized fluorescence intensity profiles were calculated and plotted. Welch's two-sample t-test
503 was used at each position along the right-left axis to determine regions of significant difference in
504 fluorescence intensity between experimental groups, indicating a change in the distribution of
505 *Tbx5*$^{+}$/*Mef2cAHF*$^{+}$ intersectional lineage cells.

506

507 **Cell Harvesting for Single Cell RNA Sequencing**

508 Samples for single cell RNA sequencing were collected from three independent litters at E13.5.
509 The heart was microdissected to obtain the interventricular septum (IVS), left ventricular (LV) and
510 right ventricular (RV) regions. Each microdissected tissue was singularized with TrypLE Express
511 (Life Technologies, Cat# 12604-013) at 37C and quenched with 1% FBS in PBS. The single cell
512 suspension was then filtered through a cell strainer cap (Corning, Cat# 352235) and centrifuged
513 at 300g for 5 minutes. The pellet was resuspended in 1% FBS in PBS and counted using an
514 automated cell counter. A 30μL aliquot of the cell suspension was used to generate single cell
515 droplet libraries with the Chromium Next GEM Single Cell 5' Library & Gel Bead Kit v1.1,

516 according to manufacturer's instructions (10X Genomics). After KAPA qPCR quantification, a
517 shallow sequencing run was performed on a NextSeq 500 (Illumina) prior to deep sequencing on
518 a NovaSeq S4 (Illumina).
519
520 **Data Processing Using Cellranger**
521 All datasets were processed using Cellranger 2.0.2. FASTQ files were generated using the
522 mkfastq function. Reads were aligned to a custom mm9 reference (version 1.2.0) containing
523 tdTomato and ZsGreen reporter genes. Cellranger aggr was used to aggregate individual libraries
524 after read depth normalization.
525
526 **Seurat Analysis**
527 Outputs from the Cellranger pipeline were analyzed using the Seurat v3 [42–44]. Datasets from the
528 IVS, LV and RV were analyzed separately. Cells with 10,000-50,000 UMIs and 1500-7250 genes
529 were retained. Data was normalized using the NormalizeData function and scaled using
530 ScaleData, while also regressing unwanted sources of variation, such as differences in the
531 number of UMIs, number of genes, percentage of mitochondrial reads and differences between
532 G2M and S phase scores. Principal component analysis (PCA) was performed using the most
533 highly variable genes. Cells were then clustered based on the top 30 principal components and
534 visualized on a Uniform Manifold Approximation and Projection (UMAP) [45]. A clustering resolution
535 that separated cells by major cell types was chosen. Next, *Tnnt2*$^{+}$ clusters from the IVS dataset
536 were extracted and re-clustered, similar to the parent dataset above. A clustering resolution was
537 chosen based on separation of genotypes. Differential gene expression tests between clusters or
538 between *ZsGreen*$^{+}$ and *ZsGreen*$^{-}$ or *tdTomato*$^{+}$ and *tdTomato*$^{-}$ cells were performed using the
539 FindMarkers function with default parameters. Selected differentially expressed genes with an
540 adjusted p-value less than 0.05 from the Wilcoxon rank sum test were displayed using the Dotplot
541 or FeaturePlot functions.

542

543 **Fluorescent *In Situ* Hybridization**

544 E11.5 or E14.5 hearts were fixed with 4% paraformaldehyde or 10% formalin overnight at 4C,
545 embedded in paraffin and then sectioned for a transverse or four-chambered view on slides. *In*
546 *situ* hybridization was performed on sections using the RNAscope Multiplex Fluorescent v2 Assay
547 kit (Advanced Cell Diagnostics, Cat# 323100). Briefly, sections were deparaffinized in xylene and
548 100% ethanol, treated with hydrogen peroxide for 10 minutes and boiled in target retrieval buffer
549 for 10 minutes. A hydrophobic barrier was drawn around each section using an Immedge pen
550 (Vector Laboratories, Cat# H-4000), and slides were allowed to dry overnight. The following day,
551 sections were treated with Protease Plus for 30 minutes, followed by hybridization with probes for
552 2 hours at 40C. Probes used were *Mm-Tnnt2-C4* (Cat# 418681-C4), *Mm-Ntn1* (Cat# 407621),
553 *Mm-Slit2* (Cat# 449691), *Mm-Nppa-C3* (Cat# 418691-C3), *Mm-Bmp2-C2* (Cat# 406661-C2), *Mm-*
554 *Robo1* (Cat# 475951) and *Mm-Unc5b* (Cat# 482481). Amplification steps were carried out
555 according to manufacturer's instructions. Opal dyes 520, 570, 620 and 690 (Akoya Biosciences,
556 Cat# FP1487001KT, FP1487001KT, FP1487001KT and FP1487001KT) were used at 1:750
557 dilution. After staining with DAPI, 1-2 drops of ProLong Gold Antifade Mountant (ThermoFisher
558 Scientific, Cat# P36930) were placed on the slides and mounted with a coverslip. Slides were
559 stored overnight at 4C and were imaged at 10X magnification on the Olympus FV3000RS. Multi-
560 Area Time Lapse (MATL) images were captured and then stitched together using the Olympus
561 FV3000RS software. Stitched images were analyzed using ImageJ OlympusViewer plugin.

562

563 **Immunohistochemistry**

564 Cryopreserved slides were thawed from -80C at RT and washed in 0.1% Triton X-100 in PBS
565 (PBST) for 3 x 5 min. Antigen-retrieval was performed by boiling slides in 10mM sodium citrate
566 buffer (pH 6.0) for 10 minutes and then washed in H2O for 3 x 5 min. Blocking was performed
567 using 5% donkey serum in 0.1% PBST at RT for 1-2hr. Anti-Netrin-1 antibody 1:500 (R&D

568 Systems AF1109) in 1% BSA + 0.1% PBST was incubated at 4C overnight. After washing 3 x 5
569 min in 0.1% PBST, slides incubated in Alexa Fluor 594 (1:300) in 1% BSA + 0.1% PBST at RT
570 for 1 hr. Slides were then washed 3 x 5 min in 0.1% PBST and incubated in 1:1000 DAPI in 0.1%
571 PBST at RT for 5-10 minutes. Finally, slides washed 3 x 5 min in 0.1% PBST, glass coverslips
572 were mounted using Prolong Gold antifade mounting medium and stored at 4C.
573

574 **Machine learning-based 3-D reconstruction from histology and quantitative micrometry**

575 Tissues were formalin-fixed, paraffin embedded (FFPE) and serially sectioned at a standard
576 thickness of 5 μm to exhaustively collect the heart tissue of each fetal mouse. Serial sections
577 were stained with hematoxylin and eosin (H&E) and digitized at 20x magnification. CODA, a
578 technique to 3-D reconstruct serial tissue images, was used to map the microanatomy of the
579 hearts [31,46]. The various steps of CODA can be broken down into image registration, nuclear
580 detection, and tissue labelling. Nonlinear image registration was used to align the serial images.
581 Cellular coordinates were generated through color deconvolution and detection of two-
582 dimensional intensity peaks in the hematoxylin channel of the images. A deep learning semantic
583 segmentation algorithm was trained to label the anatomical structures of the mice at 1 μm
584 resolution. To train the model, manual annotations of six structures were generated in 55
585 histological images corresponding to the different large structures present in the tissue: bones,
586 spinal cord, lung, liver, stroma, heart, and non-tissue pixels in the images. A second deep learning
587 model was trained to subclassify the regions of interest within the heart: compact myocardium,
588 trabeculae, IVS, AV canal and atria. Fifty images from the manual annotation datasets were used
589 for model training, with five images held out for independent testing of model accuracy. The
590 models were deemed acceptable when they reached a minimum per-class precision and recall of
591 >85%. Using the trained model, independent images were segmented and aligned to generate
592 digital 3-D datasets.

593 The reconstructed volumes enabled microanatomical quantification of anatomical
594 properties. IVS fill, or the solidity of the muscle layer in the IVS, was calculated by dividing the
595 number of dark (<200 in RBG color space) pixels within the IVS, normalized by all pixels (including
596 empty space) within the IVS. Percent trabeculation within the IVS was calculated by first isolating
597 the tissue classified as trabeculae that was spatially attached to the IVS, then normalizing this
598 number by the combined volume of trabeculae attached to IVS and the volume of the IVS itself.
599 The compact myocardium thickness was calculated by measuring the thickness of the compact
600 layer at the bottom 20% of the ventricles. To measure the thickness on the left and right ventricles,
601 the two sides of the heart were manually segmented in 3-D space. VSDs were identified by
602 calculating regions where the empty space of the left ventricle contacted the empty space of the
603 right ventricle. These defects were evaluated and manually sorted into membranous or muscular
604 sub-types. The areas of each defect were then manually calculated through annotation on serial
605 histological images representing the shortest path to close the defect. These lines were summed
606 across all images containing the defect multiplied by the thickness of the histological slides to
607 determine the area of the hole.
608
609 **Quantification and Statistical Analysis**
610 For statistical analysis of genetic interactions, the number of animals with a given defect (muscular
611 VSD or membranous VSD) was modeled in a Generalized Linear Model assuming a binomial
612 probability distribution for the observed counts. This model included main effects (in terms of log
613 odds ratios) capturing the number of mutant alleles for *Tbx5* (0 or 1, representing the WT or the
614 Het genotype, respectively) and the number of mutant alleles for *Slit2* or *Ntn1* (0,1 or 2:
615 representing the WT, Het or Hom genotype, respectively) and an interaction between these
616 effects. Given the relatively small number of animals in this experiment, bias-reduced estimates
617 were made using the brglm2 package {Kosmidis.2020} in R <https://www.R-project.org/>.
618

References

1. Cruz, M.V.D.L., Sánchez-Gómez, C., and Palomino, M.A. (1989). The primitive cardiac regions in the straight tube heart (Stage 9) and their anatomical expression in the mature heart: An experimental study in the chick embryo. J Anat *165*, 121–131.

2. Cruz, M.V. de la, Castillo, M.M., G., L.V., Valencia, A., and Moreno-Rodriguez, R.A. (1997). Primitive interventricular septum, its primordium, and its contribution in the definitive interventricular septum: In vivo labelling study in the chick embryo heart. Anatomical Rec *247*, 512–520. 10.1002/(sici)1097-0185(199704)247:4<512::aid-ar10>3.0.co;2-s.

3. Wessels, A., Vermeulen, J.L.M., Virágh, S.Z., Kálmán, F., Morris, G.E., Man, N.T., Lamers, W.H., and Moorman, A.F.M. (1990). Spatial distribution of “tissue-specific” antigens in the developing human heart and skeletal muscle. I. An immunohistochemical analysis of creatine kinase isoenzyme expression patterns. Anatomical Rec *228*, 163–176. 10.1002/ar.1092280208.

4. Wessels, A., Markman, M.W.M., Vermeulen, J.L.M., Anderson, R.H., Moorman, A.F.M., and Lamers, W.H. (1996). The Development of the Atrioventricular Junction in the Human Heart. Circ Res *78*, 110–117. 10.1161/01.res.78.1.110.

5. Lamers, W.H., Wessels, A., Verbeek, F.J., Moorman, A.F., Virágh, S., Wenink, A.C., Groot, A.C.G., and Anderson, R.H. (2018). New findings concerning ventricular septation in the human heart. Implications for maldevelopment. Circulation *86*, 1194–1205. 10.1161/01.cir.86.4.1194.

6. Devine, W.P., Wythe, J.D., George, M., Koshiba-Takeuchi, K., and Bruneau, B.G. (2014). Early patterning and specification of cardiac progenitors in gastrulating mesoderm. eLife *3*, 508. 10.7554/elife.03848.

7. Später, D., Abramczuk, M.K., Buac, K., Zangi, L., Stachel, M.W., Clarke, J., Sahara, M., Ludwig, A., and Chien, K.R. (2013). A HCN4+ cardiomyogenic progenitor derived from the first heart field and human pluripotent stem cells. Nat Cell Biol *15*, 1–10. 10.1038/ncb2824.

8. Lescroart, F., Chabab, S., Lin, X., Rulands, S., Paulissen, C., Rodolosse, A., Auer, H., Achouri, Y., Dubois, C., Bondue, A., et al. (2014). Early lineage restriction in temporally distinct populations of Mesp1 progenitors during mammalian heart development. Nat Cell Biol *16*, 829–840. 10.1038/ncb3024.

9. Meilhac, S.M., Esner, M., Kelly, R.G., Nicolas, J.-F., and Buckingham, M.E. (2004). The clonal origin of myocardial cells in different regions of the embryonic mouse heart. Dev Cell *6*, 685–698.

10. Franco, D., Meilhac, S.M., Christoffels, V.M., Kispert, A., Buckingham, M., and Kelly, R.G. (2006). Left and right ventricular contributions to the formation of the interventricular septum in the mouse heart. Dev Biol *294*, 366–375. 10.1016/j.ydbio.2006.02.045.

11. Dahmann, C., Basler, K., Dahmann, C., and Basler, K. (1999). Compartment boundaries: at the edge of development. Trends Genet *15*, 320–326. 10.1016/s0168-9525(99)01774-6.

656 12. Kiecker, C., and Lumsden, A. (2005). Compartments and their boundaries in vertebrate
657 brain development. Nat Rev Neurosci *6*, 553–564. 10.1038/nrn1702.

658 13. Wang, J., and Dahmann, C. (2020). Establishing compartment boundaries in Drosophila
659 wing imaginal discs: An interplay between selector genes, signaling pathways and cell
660 mechanics. Semin Cell Dev Biol *107*, 161–169. 10.1016/j.semcdb.2020.07.008.

661 14. Madisen, L., Garner, A.R., Shimaoka, D., Chuong, A.S., Klapoetke, N.C., Li, L.,
662 van der Bourg, A., Niino, Y., Egolf, L., Monetti, C., et al. (2015). Transgenic Mice for
663 Intersectional Targeting of Neural Sensors and Effectors with High Specificity and Performance.
664 Neuron *85*, 942–958. 10.1016/j.neuron.2015.02.022.

665 15. Wu, S., Wu, Y., and Capecchi, M.R. (2006). Motoneurons and oligodendrocytes are
666 sequentially generated from neural stem cells but do not appear to share common lineage-
667 restricted progenitors in vivo. Development *133*, 581–590. 10.1242/dev.02236.

668 16. Basson, C.T., Bachinsky, D.R., Lin, R.C., Levi, T., Elkins, J.A., Soults, J., Grayzel, D.,
669 Kroumpouzou, E., Traill, T.A., Leblanc-Straceski, J., et al. (1997). Mutations in human TBX5
670 [corrected] cause limb and cardiac malformation in Holt-Oram syndrome. Nat Genet *15*, 30–35.
671 10.1038/ng0197-30.

672 17. Li, Q.Y., Newbury-Ecob, R.A., Terrett, J.A., Wilson, D.I., Curtis, A.R., Yi, C.H., Gebuhr, T.,
673 Bullen, P.J., Robson, S.C., Strachan, T., et al. (1997). Holt-Oram syndrome is caused by
674 mutations in TBX5, a member of the Brachyury (T) gene family. Nat Genet *15*, 21–29.
675 10.1038/ng0197-21.

676 18. Kathiriya, I.S., Rao, K.S., Iacono, G., Devine, W.P., Blair, A.P., Hota, S.K., Lai, M.H., Garay,
677 B.I., Thomas, R., Gong, H.Z., et al. (2021). Modeling Human TBX5 Haploinsufficiency Predicts
678 Regulatory Networks for Congenital Heart Disease. Dev Cell *56*, 292-309.e9.
679 10.1016/j.devcel.2020.11.020.

680 19. Bruneau, B.G., Nemer, G., Schmitt, J.P., Charron, F., Robitaille, L., Caron, S., Conner, D.A.,
681 Gessler, M., Nemer, M., Seidman, C.E., et al. (2001). A murine model of Holt-Oram syndrome
682 defines roles of the T-box transcription factor Tbx5 in cardiogenesis and disease. Cell *106*, 709–
683 721. 10.1016/s0092-8674(01)00493-7.

684 20. Verzi, M.P., McCulley, D.J., Val, S.D., Dodou, E., and Black, B.L. (2005). The right ventricle,
685 outflow tract, and ventricular septum comprise a restricted expression domain within the
686 secondary/anterior heart field. Dev Biol *287*, 134–145. 10.1016/j.ydbio.2005.08.041.

687 21. Koshiba-Takeuchi, K., Mori, A.D., Kaynak, B.L., Cebra-Thomas, J., Sukonnik, T., Georges,
688 R.O., Latham, S., Beck, L., Beck, L., Henkelman, R.M., et al. (2009). Reptilian heart
689 development and the molecular basis of cardiac chamber evolution. Nature *461*, 95–98.
690 10.1038/nature08324.

691 22. Xie, L., Hoffmann, A.D., Burnicka-Turek, O., Friedland-Little, J.M., Zhang, K., and
692 Moskowitz, I.P. (2012). Tbx5-Hedgehog Molecular Networks Are Essential in the Second Heart
693 Field for Atrial Septation. Dev Cell *23*, 280–291. 10.1016/j.devcel.2012.06.006.

694 23. Mori, A.D., and Bruneau, B.G. (2004). TBX5 mutations and congenital heart disease: Holt-
695 Oram syndrome revealed. Curr Opin Cardiol *19*, 211–215.

696 24. Mommersteeg, M.T.M., Yeh, M.L., Parnavelas, J.G., and Andrews, W.D. (2015). Disrupted
697 Slit-Robo signalling results in membranous ventricular septum defects and bicuspid aortic
698 valves. Cardiovasc Res *106*, 55–66. 10.1093/cvr/cvv040.

699 25. Li, Y., Klena, N.T., Gabriel, G.C., Liu, X., Kim, A.J., Lemke, K., Chen, Y., Chatterjee, B.,
700 Devine, W., Damerla, R.R., et al. (2015). Global genetic analysis in mice unveils central role for
701 cilia in congenital heart disease. Nature *521*, 1–16. 10.1038/nature14269.

702 26. Kruszka, P., Tanpaiboon, P., Neas, K., Crosby, K., Berger, S.I., Martinez, A.F., Addissie,
703 Y.A., Pongprot, Y., Sittiwangkul, R., Silvilairat, S., et al. (2017). Loss of function in ROBO1 is
704 associated with tetralogy of Fallot and septal defects. J Med Genet *54*, 825. 10.1136/jmedgenet-
705 2017-104611.

706 27. Larrieu-Lahargue, F., Thomas, K.R., and Li, D.Y. (2012). Netrin Ligands and Receptors:
707 Lessons From Neurons to the Endothelium. Trends Cardiovas Med *22*, 44–47.
708 10.1016/j.tcm.2012.06.010.

709 28. Akerberg, B.N., Gu, F., VanDusen, N.J., Zhang, X., Dong, R., Li, K., Zhang, B., Zhou, B.,
710 Sethi, I., Ma, Q., et al. (2019). A reference map of murine cardiac transcription factor chromatin
711 occupancy identifies dynamic and conserved enhancers. Nat Commun *10*, 4907.
712 10.1038/s41467-019-12812-3.

713 29. Bin, J.M., Han, D., Sun, K.L.W., Croteau, L.-P., Dumontier, E., Cloutier, J.-F., Kania, A., and
714 Kennedy, T.E. (2015). Complete Loss of Netrin-1 Results in Embryonic Lethality and Severe
715 Axon Guidance Defects without Increased Neural Cell Death. CellReports *12*, 1099–1106.
716 10.1016/j.celrep.2015.07.028.

717 30. Lewandoski, M., Meyers, E.N., and Martin, G.R. (1997). Analysis of Fgf8 gene function in
718 vertebrate development. Cold Spring Harb Sym *62*, 159–168.

719 31. Kiemen, A.L., Braxton, A.M., Grahn, M.P., Han, K.S., Babu, J.M., Reichel, R., Jiang, A.C.,
720 Kim, B., Hsu, J., Amoa, F., et al. (2022). CODA: quantitative 3D reconstruction of large tissues
721 at cellular resolution. Nat Methods, 1–10. 10.1038/s41592-022-01650-9.

722 32. VanDusen, N.J., Casanovas, J., Vincentz, J.W., Firulli, B.A., Osterwalder, M., Lopez-Rios,
723 J., Zeller, R., Zhou, B., Grego-Bessa, J., De La Pompa, J.L., et al. (2014). Hand2 Is an Essential
724 Regulator for Two Notch-Dependent Functions within the Embryonic Endocardium. Cell Rep. *9*,
725 2071–2083. 10.1016/j.celrep.2014.11.021.

726 33. George, R.M., Firulli, B.A., Podicheti, R., Rusch, D.B., Mannion, B.J., Pennacchio, L.A.,
727 Osterwalder, M., and Firulli, A.B. (2023). Single cell evaluation of endocardial HAND2 gene
728 regulatory networks reveals critical HAND2 dependent pathways impacting cardiac
729 morphogenesis. Development *150*. 10.1242/dev.201341.

730 34. Bin, J.M., Han, D., Lai Wing Sun, K., Croteau, L.-P., Dumontier, E., Cloutier, J.-F., Kania, A.,
731 and Kennedy, T.E. (2015). Complete Loss of Netrin-1 Results in Embryonic Lethality and

732 Severe Axon Guidance Defects without Increased Neural Cell Death. Cell Reports *12*, 1099–
733 1106. 10.1016/j.celrep.2015.07.028.

734 35. Tasic, B., Hippenmeyer, S., Wang, C., Gamboa, M., Zong, H., Chen-Tsai, Y., and Luo, L.
735 (2011). Site-specific integrase-mediated transgenesis in mice via pronuclear injection. Proc
736 National Acad Sci *108*, 7902–7907. 10.1073/pnas.1019507108.

737 36. Madisen, L., Zwingman, T.A., Sunkin, S.M., Oh, S.W., Zariwala, H.A., Gu, H., Ng, L.L.,
738 Palmiter, R.D., Hawrylycz, M.J., Jones, A.R., et al. (2010). A robust and high-throughput Cre
739 reporting and characterization system for the whole mouse brain. Nat Neurosci *13*, 133–140.
740 10.1038/nn.2467.

741 37. Dominguez, M.H., Krup, A.L., Muncie, J.M., and Bruneau, B.G. (2023). Graded mesoderm
742 assembly governs cell fate and morphogenesis of the early mammalian heart. Cell *186*, 479-
743 496.e23. 10.1016/j.cell.2023.01.001.

744 38. Schindelin, J., Arganda-Carreras, I., Frise, E., Kaynig, V., Longair, M., Pietzsch, T.,
745 Preibisch, S., Rueden, C., Saalfeld, S., Schmid, B., et al. (2012). Fiji: an open-source platform
746 for biological-image analysis. Nat. Methods *9*, 676–682. 10.1038/nmeth.2019.

747 39. Kirshner, H., Aguet, F., Sage, D., and Unser, M. (2013). 3-D PSF fitting for fluorescence
748 microscopy: implementation and localization application. J. Microsc. *249*, 13–25.
749 10.1111/j.1365-2818.2012.03675.x.

750 40. Hörl, D., Rusak, F.R., Preusser, F., Tillberg, P., Randel, N., Chhetri, R.K., Cardona, A.,
751 Keller, P.J., Harz, H., Leonhardt, H., et al. (2019). BigStitcher: reconstructing high-resolution
752 image datasets of cleared and expanded samples. Nat Methods *16*, 870–874. 10.1038/s41592-
753 019-0501-0.

754 41. Tinevez, J.-Y., Perry, N., Schindelin, J., Hoopes, G.M., Reynolds, G.D., Laplantine, E.,
755 Bednarek, S.Y., Shorte, S.L., and Eliceiri, K.W. (2017). TrackMate: An open and extensible
756 platform for single-particle tracking. Methods *115*, 80–90. 10.1016/j.ymeth.2016.09.016.

757 42. Satija, R., Farrell, J.A., Gennert, D., Schier, A.F., and Regev, A. (2015). Spatial
758 reconstruction of single-cell gene expression data. Nat Biotechnol *33*, 495–502.
759 10.1038/nbt.3192.

760 43. Butler, A., Hoffman, P., Smibert, P., Papalexi, E., and Satija, R. (2018). Integrating single-
761 cell transcriptomic data across different conditions, technologies, and species. Nat Biotechnol
762 *48*, 1070–17. 10.1038/nbt.4096.

763 44. Stuart, T., Butler, A., Hoffman, P., Hafemeister, C., Papalexi, E., III, W.M.M., Hao, Y.,
764 Stoeckius, M., Smibert, P., and Satija, R. (2019). Comprehensive Integration of Single-Cell
765 Data. Cell *177*, 1–37. 10.1016/j.cell.2019.05.031.

766 45. Becht, E., McInnes, L., Healy, J., Dutertre, C.-A., Kwok, I.W.H., Ng, L.G., Ginhoux, F., and
767 Newell, E.W. (2018). Dimensionality reduction for visualizing single-cell data using UMAP. Nat
768 Biotechnol. 10.1038/nbt.4314.

46. Forjaz, A., Vaz, E., Romero, V.M., Joshi, S., Braxton, A.M., Jiang, A.C., Fujikura, K., Cornish, T., Hong, S.-M., Hruban, R.H., et al. (2023). Three-dimensional assessments are necessary to determine the true spatial tissue composition of diseased tissues. bioRxiv, 2023.12.04.569986. 10.1101/2023.12.04.569986.

Acknowledgements. We thank Brian Black for mouse lines and members of the Bruneau lab for troubleshooting help, discussions and comments. We also thank the Gladstone Bioinformatics, Genomics, and Histology and Microscopy Cores, the UCSF Laboratory for Cell Analysis, and the UCSF Center for Advanced Technology. This work was supported by grants from the National Institutes of Health (NHLBI Bench to Bassinet Program UM1HL098179 to B.G.B.; R01HL114948 to B.G.B., R01HL155906 to B.G.B. and I.S.K., U54CA268083 and UG3CA275681 to A.L.K.), Additional Ventures to B.G.B., Society for Pediatric Anesthesia (Young Investigator Award to I.S.K.), Hellman Family Fund (I.S.K.), UCSF REAC Grant (I.S.K.), UCSF Pediatric Heart Center Catalyst Award to I.S.K. and UCSF Department of Anesthesia and Perioperative Care (Ongoing Investigator Award to I.S.K.). This work was also supported by an NIH/NCRR grant (C06 RR018928) to the J. David Gladstone Institutes, and the Younger Family Fund (B.G.B.).

Author Contributions. W.P.D. and B.G.B. originally conceived, and I.S.K. and B.G.B. refined and developed the study. W.P.D. made initial observations using genetic lineage tools that he gathered or generated, such as *ROSA26*^{Ai66b} and the intersectional-*DTA*. I.S.K., M.H.D., W.P.D. and K.M.H. performed embryo dissections. K.M.H., B.I.G., P.G., M.N.M., T.S., D.M.P., S.W. and E.F.B. managed animal husbandry and genotyping. I.S.K., M.H.D., W.P.D. and K.M.H. performed whole mount or section immunostaining experiments and imaging. M.H.D., J.M.M. and D.Q performed lightsheet imaging and processing, and M.H.D. and J.M.M. implemented analyses with hypothesis-based input from I.S.K. I.S.K. designed strategy to use 5’ sequencing kit and developed synthetic genome with Gladstone Bioinformatics core, micro-dissected heart regions for scRNA-seq and processed samples with K.S.R. and P.G. for sequencing library

preparations. K.S.R. generated scRNA-seq libraries and performed scRNA-seq analyses with hypothesis-based input from I.S.K. K.S.R., K.M.H., P.G. and M.N.M. performed section *in situ* hybridization and imaging. K.S.R. generated ChIP-seq browser tracks with input from S.H. I.S.K. assessed cardiac defects by histology and provided anatomical knowledge to A.L.K. to apply a deep learning tool for cardiac morphometry. A.F. trained deep learning models and was supervised by A.L.K. and advised by P-H.W. and D.W. B.G.B. supervised and advised the study. I.S.K. and K.S.R. prepared figures. I.S.K. wrote the original draft with contributions from co-authors. I.S.K. and B.G.B. reviewed and edited the manuscript with input from co-authors.

Declaration of Interests: B.G.B. is a co-founder and shareholder of Tenaya Therapeutics. B.G.B. is an advisor for Silver Creek Pharmaceuticals. None of the work presented here is related to these commercial interests.

Figure 1

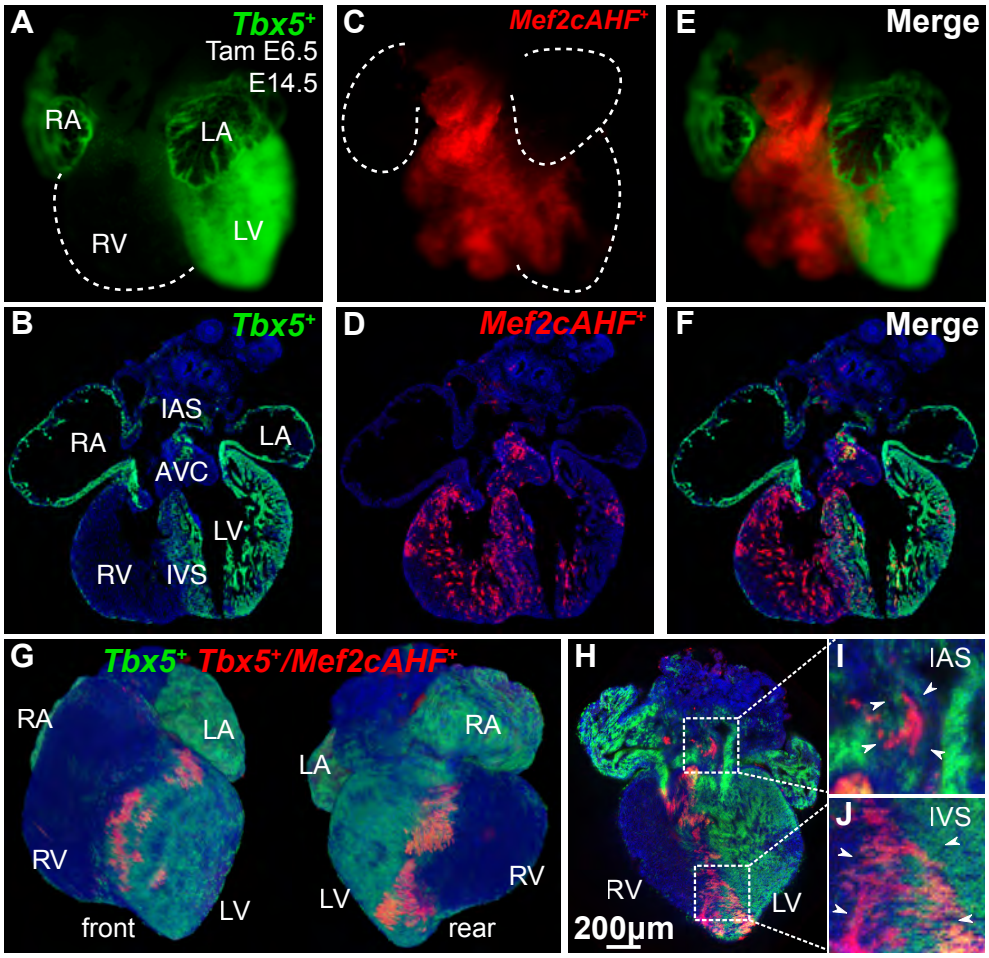
A
Tbx5+
Tam E6.5
E14.5
RA
LA
RV
LV
C
Mef2cAHF+
E
Merge
B
Tbx5+
IAS
RA
LA
AVC
LV
RV
IVS
D
Mef2cAHF+
F
Merge
G
Tbx5+ Tbx5+/Mef2cAHF+
RA
LA
RV
LV
front
RA
LA
RV
LV
rear
H
RV
LV
200µm
I
IAS
J
IVS

Figure 1. *Tbx5*$^{+}$/*Mef2cAHF*$^{+}$ lineage marks a compartment boundary at the cardiac interventricular septum At E14.5, (A, B) clonal cell descendants of a *Tbx5*$^{+}$ lineage (ZsGreen) labeled at E6.5 contributes to the LV, and (C, D) a *Mef2cAHF*$^{+}$ lineage (tdTomato immunostaining) contributes to the RV, demonstrating largely complementary patterns. (F-J) These lineages overlap (*Tbx5*$^{+}$/*Mef2cAHF*$^{+}$) at the interventricular septum (IVS), as well as the atrioventricular canal (AVC) and interatrial septum (IAS). *Tbx5*$^{CreERT2/+}$; *Mef2cAHF-DreERT2*; *Rosa26*$^{Ai6/Ai66b}$ hearts by epifluorescence microscopy (A-C) and cryosections (D-F). (G-J) Maximal projection images by light sheet microscopy of an intersectional reporter for the *Tbx5*$^{+}$/*Mef2cAHF*$^{+}$ lineage (tdTomato immunostaining) in *Tbx5*$^{CreERT2/+}$; *Mef2cAHF-DreERT2*; *Rosa26*$^{Ai66/+}$ embryos.

Figure S1

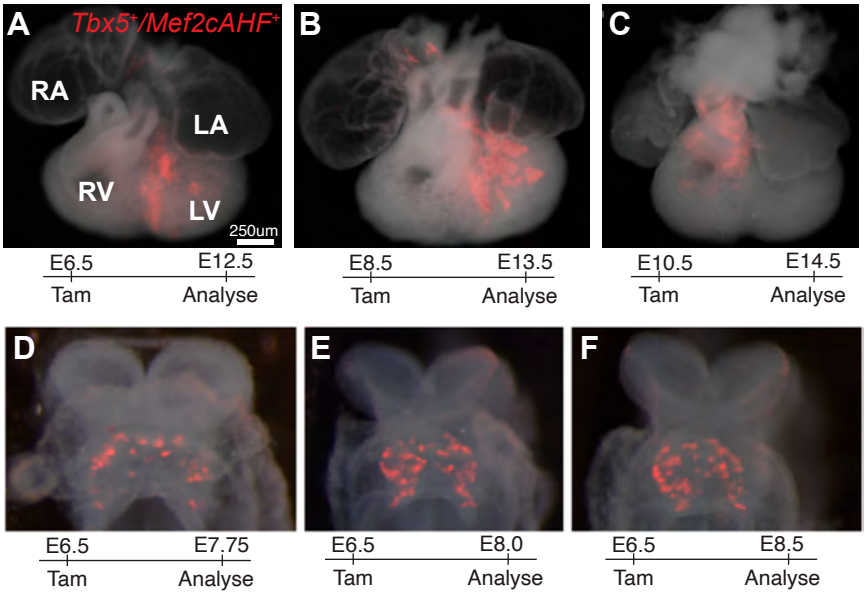
A
Tbx5+/Mef2cAHF+
RA
LA
RV
LV
250um
B
C
E6.5
E12.5
Tam
Analyse
E8.5
E13.5
Tam
Analyse
E10.5
E14.5
Tam
Analyse
D
E
F
E6.5
E7.75
Tam
Analyse
E6.5
E8.0
Tam
Analyse
E6.5
E8.5
Tam
Analyse

11 **Supplemental Figure 1.** (A-C) *Tbx5*$^{+}$*/Mef2cAHF*$^{+}$ lineage contributions to the interventricular
12 septum were descendants from progenitors labeled at (A) E6.5, but not at (B) E8.5 or (C) E10.5
13 in *Tbx5*$^{CreERT2/+}$; *Mef2cAHF-DreERT2*; *Rosa26*$^{Ai6/Ai66}$ embryos. Epifluorescence microscopy
14 images of the *Tbx5*$^{+}$*/Mef2cAHF*$^{+}$ lineage (tdTomato immunostaining) labeled at E6.5 from (A)
15 E7.75, (B) E8.0 and (C) E8.5 displayed an apparent "salt and pepper" pattern in the early
16 developing heart.
17

Figure 2

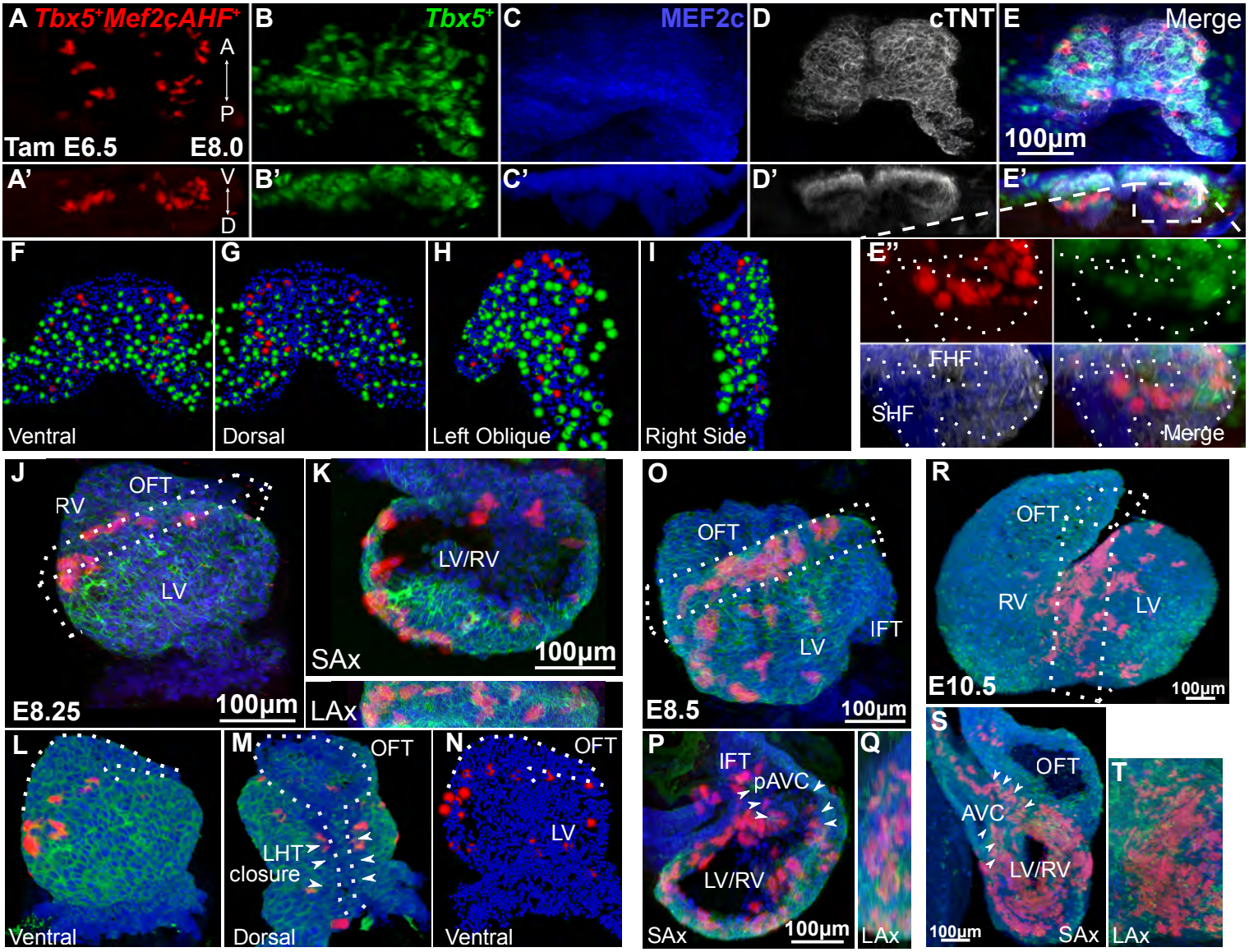
A Tbx5+Mef2cAHF+
A
P
Tam E6.5
E8.0
B Tbx5+
C MEF2c
D cTNT
E Merge
100µm
A'
V
D
B'
C'
D'
E'
F
Ventral
G
Dorsal
H
Left Oblique
I
Right Side
E''
FHF
SHF
Merge
J
RV
OFT
LV
E8.25
100µm
K
LV/RV
SAx
100µm
LAx
O
OFT
IFT
LV
E8.5
100µm
R
OFT
RV
LV
E10.5
100µm
L
Ventral
M
OFT
LHT
closure
Dorsal
N
OFT
LV
Ventral
P
IFT
pAVC
LV/RV
SAx
100µm
Q
LAx
S
OFT
AVC
LV/RV
100µm
SAx
T
LAx

Figure 2. *Tbx5*$^{+}$*/Mef2cAHF*$^{+}$ lineage is prefigured in early mouse heart development. Frontal (A-E), transverse (A'-E') and magnified transverse (E'') views of maximum Z-projections of whole mount embryos by lightsheet imaging at E8.0 show the *Tbx5*$^{+}$ lineage (ZsGreen), and immunostaining of tdTomato for the *Tbx5*$^{+}$*/Mef2cAHF*$^{+}$ lineage, MEF2c and cTNT in *Tbx5*$^{CreERT2/+}$; *Mef2cAHF-DreERT2*; *Rosa26*$^{Ai6/Ai66}$ embryos. A-P, anterior-posterior axis; V-D, ventral-dorsal axis. First (FHF) and second (SHF) heart fields. At E8.0 (approximately 3 somites), *Tbx5*$^{+}$ lineage cells are restricted to a ventral domain corresponding to the FHF, whereas *Tbx5*$^{+}$*/Mef2cAHF*$^{+}$ lineage cells originate along the FHF-SHF boundary. *Tbx5*$^{+}$*/Mef2cAHF*$^{+}$ lineage cells lie in an apparent planar ringlet in the dorsal-ventral axis that expands as the heart tube grows. (J-N) At E8.25 (approximately 6 somites), with dorsal closure of the linear heart tube (LHT) underway, the *Tbx5*$^{+}$*/Mef2cAHF*$^{+}$ lineage cells form a ring situated between the RV and LV primordia, which is observed from multiple perspectives including anterior, short-axis (SAx) and long-axis (LAx) views. (O-Q) At E8.5 (approximately 9 somites), *Tbx5*$^{+}$*/Mef2cAHF*$^{+}$ lineage cells are observed in a portion of the AVC primoridium (pAVC and arrowheads). (R-T) At E10.5, a band of *Tbx5*$^{+}$*/Mef2cAHF*$^{+}$ lineage cells extends from the interventricular groove at the outer curvature to the inner curvature of the heart. SAx and LAx show that *Tbx5*$^{+}$*/Mef2cAHF*$^{+}$ lineage cells occupies a crossroads for heart morphogenesis, spanning the growing interventricular septum to the AVC, adjacent to the OFT.

Figure S2

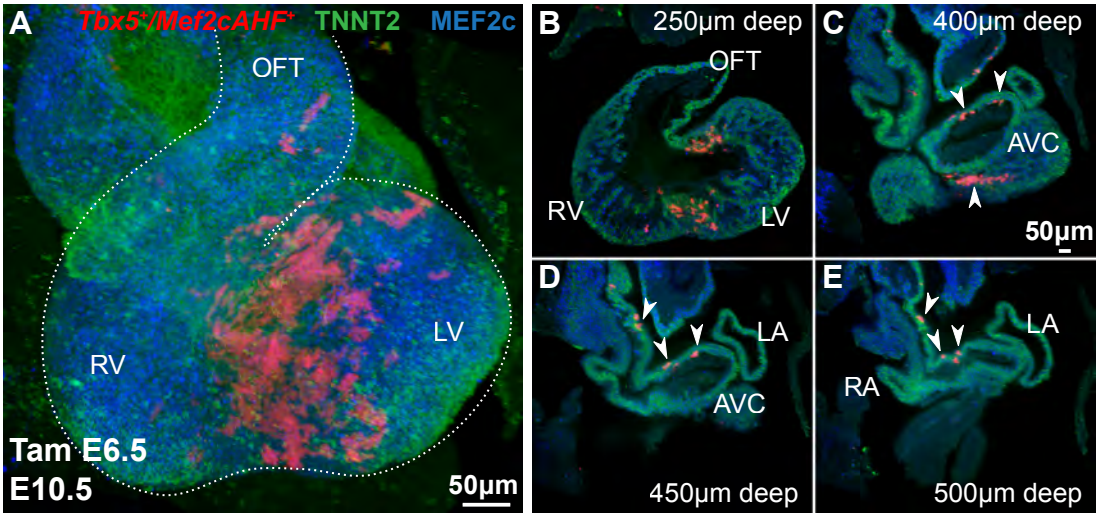
A
Tbx5+/Mef2cAHF+
TNNT2
MEF2c
OFT
RV
LV
Tam E6.5
E10.5
50μm
B
250μm deep
OFT
RV
LV
C
400μm deep
AVC
50μm
D
LA
AVC
450μm deep
E
LA
RA
500μm deep

Supplemental Figure 2. (A-E) In the developing atria, optical sections from ventral to dorsal show lineage-labeled *Tbx5*$^{+}$*/Mef2cAHF*$^{+}$ lineage cells from the AV cushion (AVC) region to the roof of the atrium, prior to the formation of the interatrial septum, in *Tbx5*$^{CreERT2/+}$; *Mef2cAHF-DreERT2*; *Rosa26*$^{Ai6/Ai66}$ embryos.

Figure 3

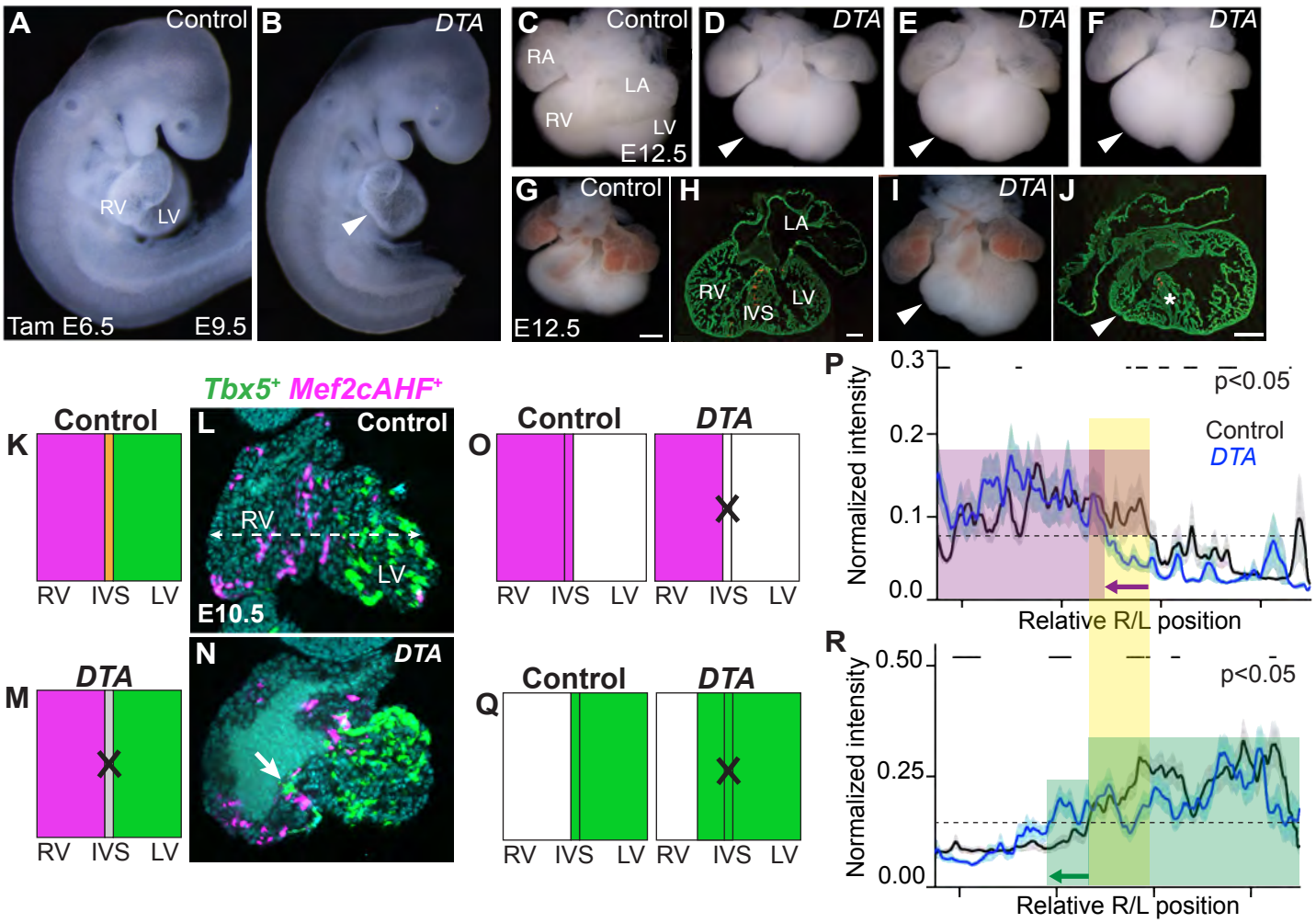
A
Control
RV
LV
Tam E6.5
E9.5
B
DTA
C
Control
RA
LA
RV
LV
E12.5
D
DTA
E
DTA
F
DTA
G
Control
E12.5
H
LA
RV
IVS
LV
I
DTA
J
*
Tbx5+ Mef2cAHF+
K
Control
RV IVS LV
L
Control
RV
LV
E10.5
M
DTA
RV IVS LV
N
DTA
O
Control
DTA
RV IVS LV RV IVS LV
Q
Control
DTA
RV IVS LV RV IVS LV
P
Normalized intensity
0.3
0.2
0.1
0.0
p<0.05
Control
DTA
Relative R/L position
R
Normalized intensity
0.50
0.25
0.00
p<0.05
Relative R/L position

Figure 3. Cell ablation of *Tbx5*$^{+}$/*Mef2cAHF*$^{+}$ progenitors causes RV hypoplasia, IVS disorganization, and lineage mixing. Misexpression of *diphtheria toxin* (*DTA*) in *Tbx5*$^{+}$/*Mef2cAHF*$^{+}$ progenitors in *Tbx5*$^{CreERT2/+}$; *Mef2cAHF-DreERT2*; *Rosa26*$^{Ai66/+}$; *Hip11*$^{intersectional-DTA/+}$ embryos (*DTA*), compared to *Tbx5*$^{CreERT2/+}$; *Mef2cAHF-DreERT2*; *Rosa26*$^{Ai66/+}$; *Hip11*$^{+/+}$ (control), resulted in RV hypoplasia (arrows) at E9.5 (A, B), and E12.5 (C-J), along with disorganization and non-compaction of the interventricular septum (IVS) (asterisk) (G-J). (K-N) At E10.5, mixing of the *Mef2cAHF*$^{+}$ lineage and *Tbx5*$^{+}$ lineage (white arrow in N shows ectopic *Tbx5*$^{+}$ lineage ZsGreen cell in the right heart) was observed by lightsheet microscopy in *Tbx5*$^{CreERT2/+}$; *Mef2cAHF-DreERT2*; *Rosa26*$^{Ai6/Ai66b}$; *Hip11*$^{intersectional-DTA/+}$ embryos (*DTA*) (n=2) compared to *Tbx5*$^{CreERT2/+}$; *Mef2cAHF-DreERT2*; *Rosa26*$^{Ai6/Ai66b}$; *Hip11*$^{+/+}$ embryos (control) (n=2). (O-R) Linear profiles quantified fluorescence intensity above a threshold (dashed line in P,R) across the heart at the right or left (R/L) positions. *Mef2cAHF*$^{+}$ lineage retreated rightward (depiction in O, purple arrow in P) while *Tbx5*$^{+}$ lineage cells expanded rightward into the RV (depiction in Q, green arrow in R), consistent with a compartment boundary disruption. Yellow shading represents *Tbx5*$^{+}$/*Mef2cAHF*$^{+}$ lineage cells and region of cell ablation. Statistical significance ($p<0.05$) between control and *DTA* mutants was determined by Welch's two-sample t-test at each position along the right-left axis.

Figure S3

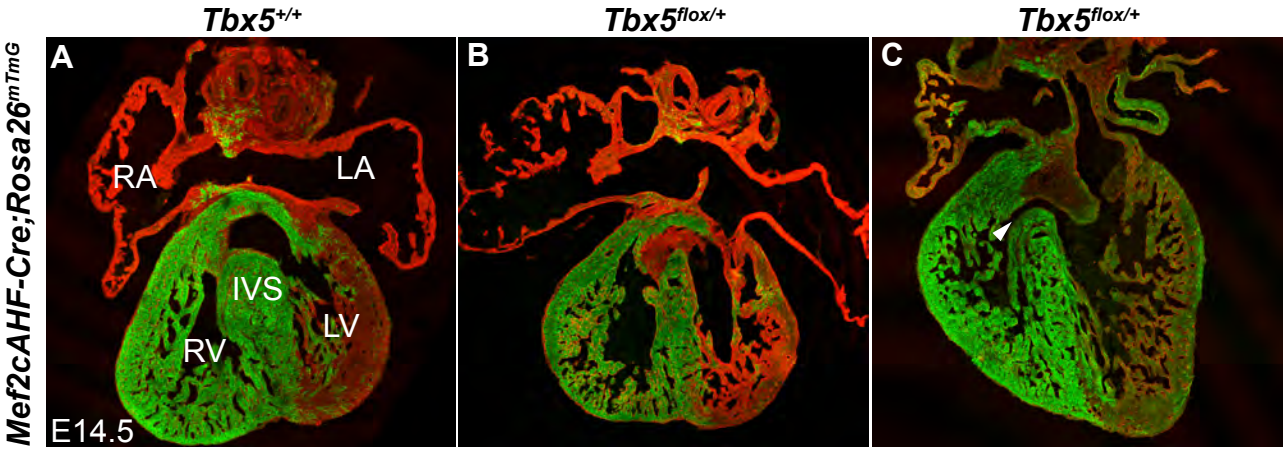
Tbx5+/+
Tbx5flox/+
Tbx5flox/+
Mef2cAHF-Cre;Rosa26mTmG
A
B
C
RA
LA
IVS
LV
RV
E14.5

Supplemental Figure 3. Conditional haploinsufficiency of *Tbx5* in the interventricular septum (IVS) leads to ventricular septal defects (VSDs). (A-C) At E14.5, membranous VSDs were observed in *Mef2cAHF-Cre*;*ROSA26*$^{mTmG/+}$;*Tbx5*$^{flox/+}$ mutant embryos (n=4/7) compared to *Mef2cAHF-Cre*;*ROSA26*$^{mTmG/+}$;*Tbx5*$^{flox/+}$ controls (n=0/3).

Figure 4

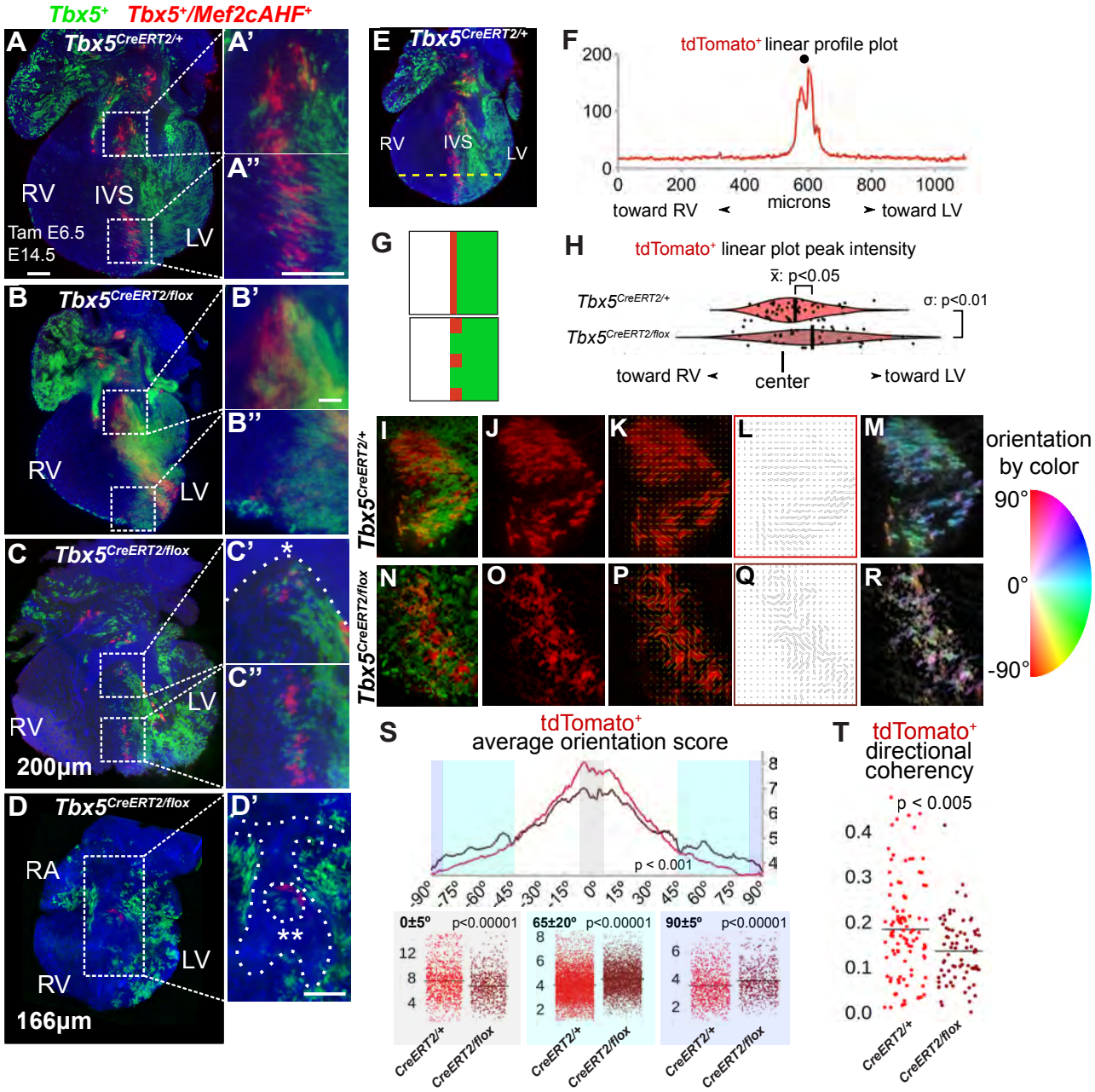
Tbx5+ Tbx5+/Mef2cAHF+
A Tbx5CreERT2/+
A'
A''
RV
IVS
LV
Tam E6.5
E14.5
B Tbx5CreERT2/flox
B'
B''
RV
LV
C Tbx5CreERT2/flox
C'
C''
RV
LV
200µm
D Tbx5CreERT2/flox
D'
RA
RV
LV
166µm
E Tbx5CreERT2/+
RV
IVS
LV
F
tdTomato+ linear profile plot
200
100
0
0 200 400 600 800 1000
microns
toward RV
toward LV
G
H
tdTomato+ linear plot peak intensity
x̄: p<0.05
σ: p<0.01
Tbx5CreERT2/+
Tbx5CreERT2/flox
toward RV
center
toward LV
I J K L M
N O P Q R
Tbx5CreERT2/+
Tbx5CreERT2/flox
orientation by color
90°
0°
-90°
S
tdTomato+ average orientation score
p < 0.001
-90° -75° -60° -45° -30° -15° 0° 15° 30° 45° 60° 75° 90°
0±5° p<0.00001
65±20° p<0.00001
90±5° p<0.00001
CreERT2/+
CreERT2/flox
T
tdTomato+ directional coherency
p < 0.005
0.4
0.3
0.2
0.1
0.0
CreERT2/+
CreERT2/flox

Figure 4. Reduced Tbx5 dosage caused ventricular septal defects and perturbations to IVS boundary position and integrity. (A) Mid-posterior optical sections from light sheet microscopy of a control (*Tbx5*$^{CreERT2/+}$;*Mef2cAHF-DreERT2*;*ROSA26*$^{Ai6/Ai66}$) heart display *Tbx5*$^{+}$ lineage (ZsGreen) and *Tbx5*$^{+}$/*Mef2cAHF*$^{+}$ lineage (tdTomato immunostaining) cells. *Tbx5*$^{+}$/*Mef2cAHF*$^{+}$ lineage cells in the interventricular septum (IVS) extended from the base (A') to the apex (A") of the heart, where cells were highly organized. (B-D) A spectrum of phenotypes of *Tbx5*$^{CreERT2/flox}$ mutants (*Tbx5*$^{CreERT2/flox}$;*Mef2cAHF-DreERT2*;*ROSA26*$^{Ai6/Ai66}$) were observed, including intact IVS (B-B"), membranous VSD (C-C", asterisk) and atrioventricular septal defect (double asterisk in D'). (B', B", C', C", D') A reduction, maldistribution and disorientation of *Tbx5*$^{+}$/*Mef2cAHF*$^{+}$ lineage cells were observed in *Tbx5*$^{CreERT2/flox}$ mutants. (E-H) Linear plot profiles at positions along the anterior-posterior and apical-basal axis of control (n=4) and *Tbx5*$^{CreERT2/flox}$ mutant (n=3) hearts for *Tbx5*$^{+}$/*Mef2cAHF*$^{+}$ lineage cells showed a leftward shift of boundary positioning and broadening of the *Tbx5*$^{+}$/*Mef2cAHF*$^{+}$ lineage position, consistent with lineage mixing. (E,F) An example of a linear profile plot is shown, and (G,H) aggregated data is depicted and quantified. (I-T) Orientation scores for cells from each channel (tdTomato^{+} or ZsGreen^{+}) was delineated for each genotype, and distributions were plotted as a function of angle. *Tbx5*$^{CreERT2/flox}$ mutant hearts scored worse for orientation of *Tbx5*$^{+}$/*Mef2cAHF*$^{+}$ lineage (tdTomato^{+}) cells in the dominant direction (range from -5 to 5 degrees) and scored higher in the orientation orthogonal to the dominant direction (range from 85 to 95 degrees and -85 to -95 degrees), as determined (S) by Watson's two-sample test across all orientations or by Wilcoxon signed-rank test for selected orientations. (T) *Tbx5*$^{+}$/*Mef2cAHF*$^{+}$ lineage (tdTomato^{+}) cells demonstrated worse directional coherency scoring in *Tbx5*$^{CreERT2/flox}$ mutants by Wilcoxon signed-rank test.

Figure S4

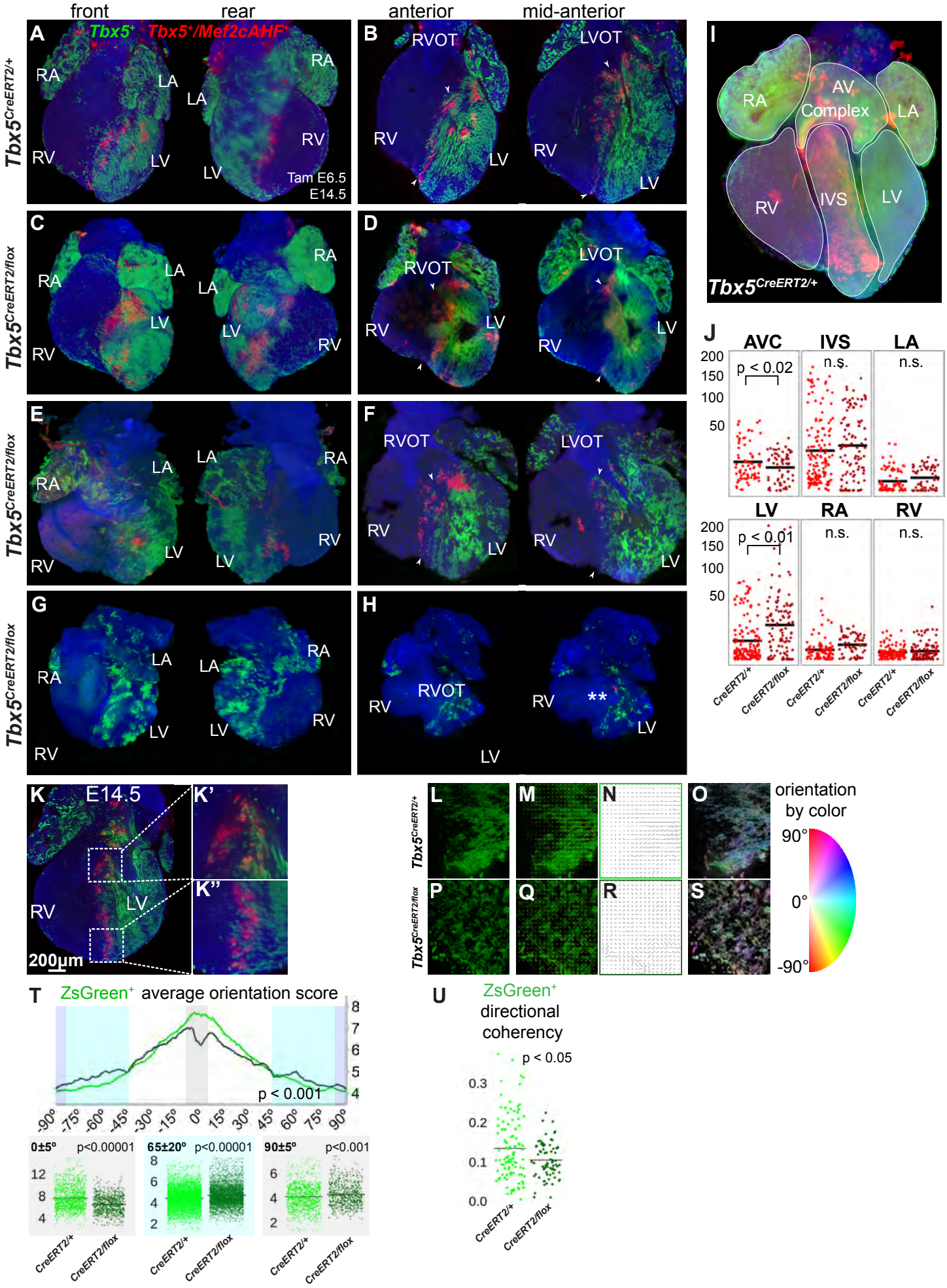
front
rear
anterior
mid-anterior
A
Tbx5+
Tbx5+/Mef2cAHF+
RA
LA
RV
LV
Tam E6.5
E14.5
B
RVOT
LVOT
C
D
E
F
G
H
**
I
AV
Complex
IVS
Tbx5CreERT2/+
Tbx5CreERT2/flox
J
AVC
IVS
LA
LV
RA
RV
p < 0.02
p < 0.01
n.s.
CreERT2/+
CreERT2/flox
K
E14.5
K'
K''
200µm
L
M
N
O
P
Q
R
S
orientation
by color
90°
0°
-90°
T
ZsGreen+ average orientation score
p < 0.001
0±5°
p<0.00001
65±20°
p<0.00001
90±5°
p<0.001
U
ZsGreen+
directional
coherency
p < 0.05

Supplemental Figure 4. (A-H) Volume renderings from lightsheet microscopy of anterior and posterior surfaces, as well as anterior and mid-anterior 4-chamber optical sections of *Tbx5*$^{CreERT2/+}$ control (*Tbx5*$^{CreERT2/+}$;*Mef2cAHF-DreERT2*;*ROSA26*$^{Ai6/Ai66}$) and *Tbx5*$^{CreERT2/flox}$ mutant (*Tbx5*$^{CreERT2/flox}$*;Mef2cAHF-DreERT2*;*ROSA26*$^{Ai6/Ai66}$) hearts at E14.5 display *Tbx5*$^{+}$ lineage (ZsGreen) and *Tbx5*$^{+}$*/Mef2cAHF*$^{+}$ lineage (tdTomato immunostaining) cells. (I, J) Quantification of the anatomical location of tdTomato^{+} and ZsGreen^{+} cells in *Tbx5*$^{CreERT2/flox}$ mutants (n=4) and *Tbx5*$^{CreERT2/+}$ controls (n=4), by region as outlined in (I). Over 1200 3-dimensional regions of interest were drawn blinded, and then integrated fluorescence signal was assessed. (J) Although no regional differences in the intensities of ZsGreen^{+} were detected, tdTomato^{+} displayed higher integrated fluorescence in the left ventricle (LV) and less signal in atrioventricular canal (AVC) by Wilcoxon signed-rank test. (L-U) *Tbx5*$^{CreERT2/flox}$ mutant hearts scored worse for orientation scores of *Tbx5*$^{+}$ lineage (ZsGreen^{+}) cells in the dominant direction (range from -5 to 5 degrees) and scored higher in the orientation orthogonal to the dominant direction (range from 85 to 95 degrees and -85 to -95 degrees), as determined (T) by Watson's two-sample test across all orientations or by Wilcoxon signed-rank test for selected orientations. (U) *Tbx5*$^{+}$ lineage (ZsGreen^{+}) cells demonstrated worse directional coherency scoring in *Tbx5*$^{CreERT2/flox}$ mutants by Wilcoxon signed-rank test.

Figure 5

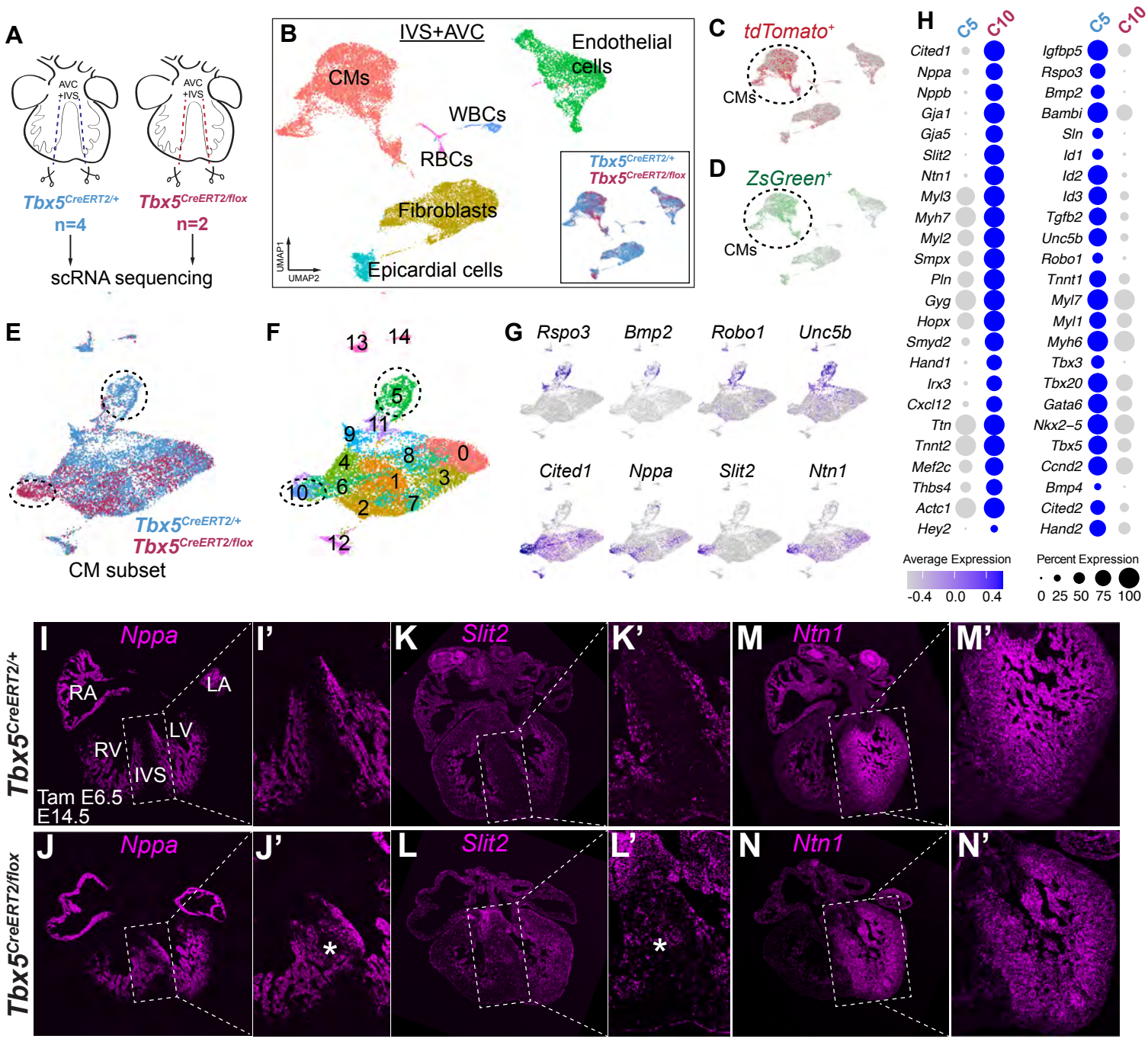
A
AVC
+IVS
Tbx5CreERT2/+
n=4
Tbx5CreERT2/flox
n=2
scRNA sequencing
B
IVS+AVC
CMs
Endothelial cells
WBCs
RBCs
Fibroblasts
Epicardial cells
UMAP1
UMAP2
Tbx5CreERT2/+
Tbx5CreERT2/flox
C
tdTomato+
CMs
D
ZsGreen+
CMs
E
Tbx5CreERT2/+
Tbx5CreERT2/flox
CM subset
F
13
14
5
11
9
4
8
0
10
6
1
3
2
7
12
G
Rspo3
Bmp2
Robo1
Unc5b
Cited1
Nppa
Slit2
Ntn1
H
C5
C10
Cited1
Nppa
Nppb
Gja1
Gja5
Slit2
Ntn1
Myl3
Myh7
Myl2
Smpx
Pln
Gyg
Hopx
Smyd2
Hand1
Irx3
Cxcl12
Ttn
Tnnt2
Mef2c
Thbs4
Actc1
Hey2
Igfbp5
Rspo3
Bmp2
Bambi
Sln
Id1
Id2
Id3
Tgfb2
Unc5b
Robo1
Tnnt1
Myl7
Myl1
Myh6
Tbx3
Tbx20
Gata6
Nkx2–5
Tbx5
Ccnd2
Bmp4
Cited2
Hand2
Average Expression
-0.4
0.0
0.4
Percent Expression
0
25
50
75
100
Tbx5CreERT2/+
Tbx5CreERT2/flox
I
Nppa
RA
LA
LV
RV
IVS
Tam E6.5
E14.5
I'
K
Slit2
K'
M
Ntn1
M'
J
Nppa
J'
*
L
Slit2
L'
*
N
Ntn1
N'

Figure 5. *Slit2* and *Ntn1* are *Tbx5*-sensitive genes in the interventricular septum (IVS). (A) At E13.5, we micro-dissected the right ventricle (RV), left ventricle (LV) and IVS+atrioventricular canal (AVC) in *Tbx5*$^{CreERT2/+}$ controls (*Tbx5*$^{CreERT2/+}$;*Mef2cAHF-DreERT2*;*ROSA26*$^{Ai6/Ai66}$)(n=4) and *Tbx5*$^{CreERT/flox}$ mutants (*Tbx5*$^{CreERT2/flox}$*;Mef2cAHF-DreERT2*;*ROSA26*$^{Ai6/Ai66}$)(n=2) with the labeled *Tbx5*$^{+}$*/Mef2cAHF*$^{+}$ lineage (*tdTomato*$^{+}$) and *Tbx5*$^{+}$ lineage (*ZsGreen*$^{+}$) cells, after tamoxifen at E6.5. (B) UMAP visualization by cell type clusters and *Tbx5* genotype (inset). CMs, cardiomyocytes; WBCs, white blood cells; RBCs, red blood cells. (C) *ZsGreen*$^{+}$ and (D) *tdTomato*$^{+}$ cells are enriched among CMs. (E) UMAP shows a *Tnnt2*$^{+}$ CM subset by *Tbx5* genotype or (F) Louvain clusters. (G) Feature plots show that atrioventricular canal genes (*Rspo3, Bmp2, Robo1, Unc5b*) are enriched among control-enriched cluster 5, suggesting downregulation of these genes in *Tbx5* mutants. Trabecular genes (*Cited1, Nppa, Slit2, Ntn1*) were enriched in the *Tbx5* mutant-enriched cluster 10. (H) Dot plots of selected genes that are upregulated in cluster 10 (C10) or in cluster 5 (C5). Significance of adj $p<0.05$ was determined by Wilcoxan rank sum. (I-N) Fluorescent *in situ* hybridization of trabecular genes *Nppa*, *Slit2* and *Ntn1* in *Tbx5*$^{CreERT2/+}$ controls or *Tbx5*$^{CreERT2/flox}$ mutants at E14.5. (I, K) *Nppa* and *Slit2* are normally expressed in the ventricular trabecular layer and excluded from the core of the IVS. (J, L) In a *Tbx5*$^{CreERT2/flox}$ mutant with an intact IVS, *Nppa* and *Slit2* are misexpressed in the IVS (asterisk). (M) *Ntn1* is normally expressed in the trabecular layer and in a gradient across the IVS, from left to right. (N) In a *Tbx5*$^{CreERT2/flox}$ mutant with an intact IVS, *Ntn1* is expanded across the IVS, flattening its gradient.

Figure S5

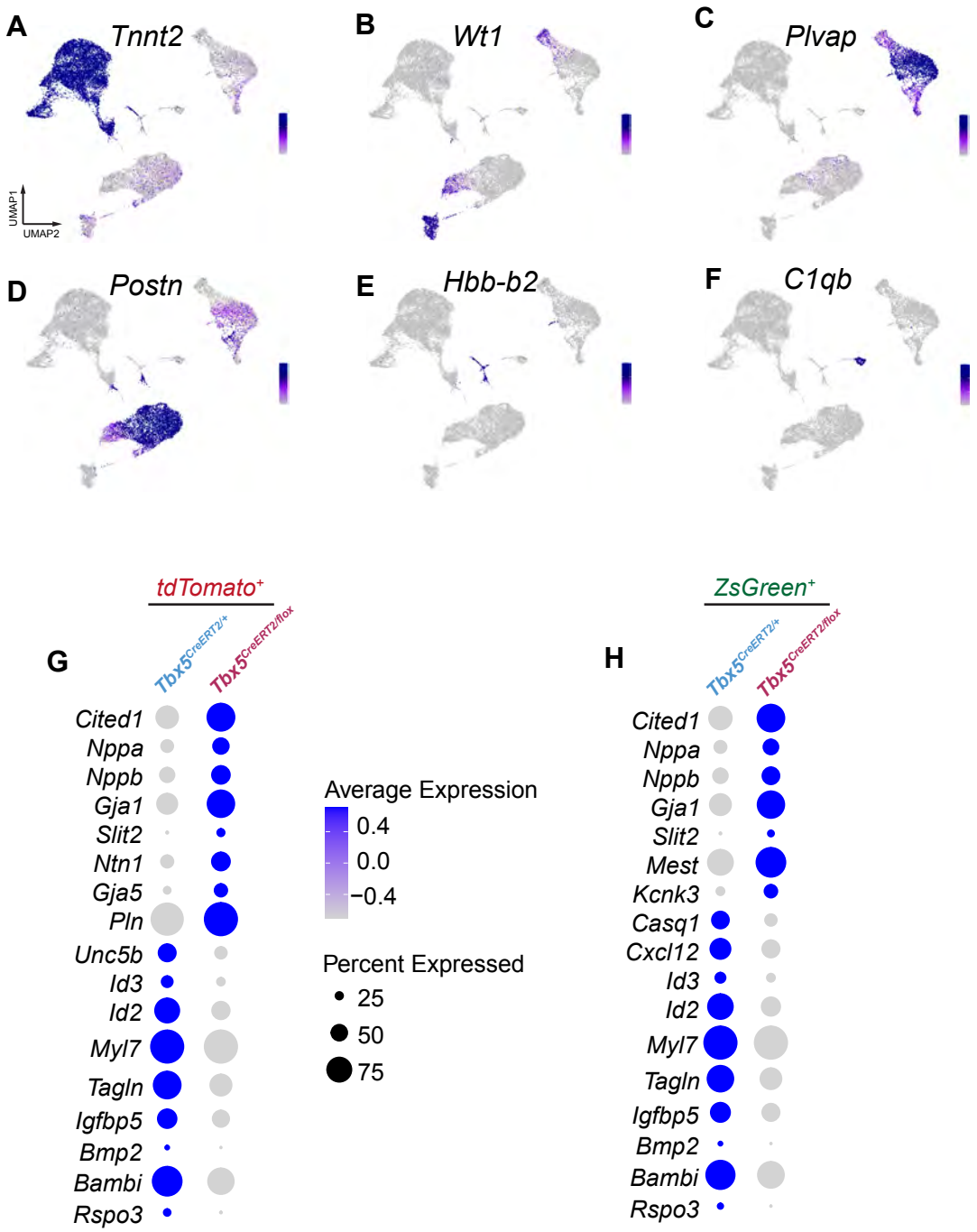
A
Tnnt2
B
Wt1
C
Plvap
D
Postn
E
Hbb-b2
F
C1qb
UMAP1
UMAP2
G
tdTomato+
Tbx5CreERT2/+
Tbx5CreERT2/flox
Cited1
Nppa
Nppb
Gja1
Slit2
Ntn1
Gja5
Pln
Unc5b
Id3
Id2
Myl7
Tagln
Igfbp5
Bmp2
Bambi
Rspo3
Average Expression
0.4
0.0
−0.4
Percent Expressed
25
50
75
H
ZsGreen+
Tbx5CreERT2/+
Tbx5CreERT2/flox
Cited1
Nppa
Nppb
Gja1
Slit2
Mest
Kcnk3
Casq1
Cxcl12
Id3
Id2
Myl7
Tagln
Igfbp5
Bmp2
Bambi
Rspo3

Supplemental Figure 5. In scRNA-seq samples from the IVS+AVC region, we detected clusters enriched for (A) *Tnnt2*$^{+}$ cardiomyocytes (CMs), (B) *Tbx18*$^{+}$*/Wt1*$^{+}$ epicardial cells, (C) *Plvap*$^{+}$ endothelial cells, (D) *Postn*$^{+}$ fibroblasts, (E) *Hbb-b2*$^{+}$ red blood cells, and (F) *C1qb*$^{+}$ white blood cells. Dot plots of selected differentially expressed genes in (G) *tdTomato*$^{+}$ or (H) *ZsGreen*$^{+}$ cells. Significance of adj $p<0.05$ was determined by Wilcoxan rank sum.

Figure S6

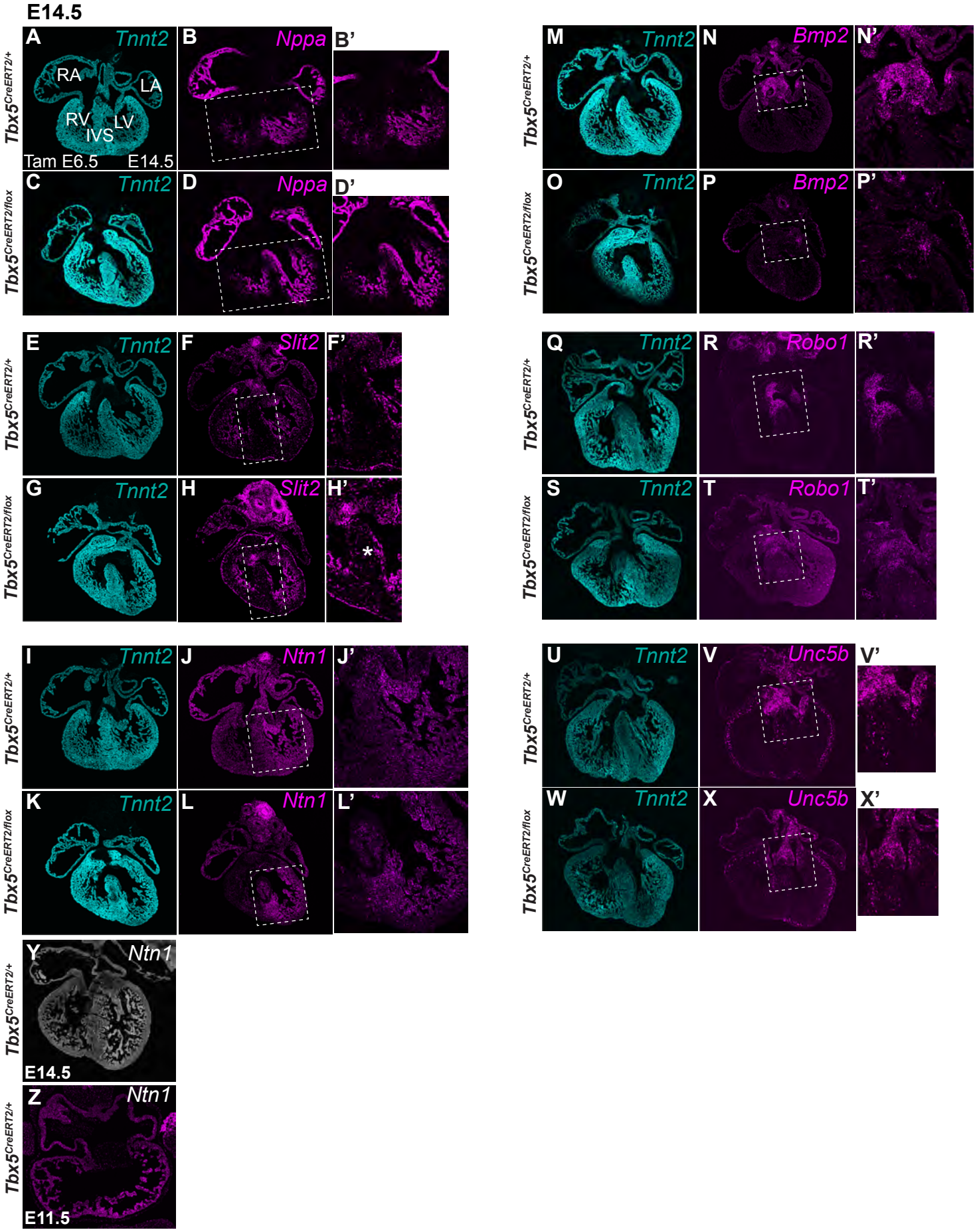
E14.5
A
Tnnt2
RA
LA
RV
LV
IVS
Tam E6.5
E14.5
B
Nppa
B'
C
Tnnt2
D
Nppa
D'
M
Tnnt2
N
Bmp2
N'
O
Tnnt2
P
Bmp2
P'
E
Tnnt2
F
Slit2
F'
G
Tnnt2
H
Slit2
H'
*
Q
Tnnt2
R
Robo1
R'
S
Tnnt2
T
Robo1
T'
I
Tnnt2
J
Ntn1
J'
K
Tnnt2
L
Ntn1
L'
U
Tnnt2
V
Unc5b
V'
W
Tnnt2
X
Unc5b
X'
Y
Ntn1
E14.5
Z
Ntn1
E11.5
Tbx5CreERT2/+
Tbx5CreERT2/flox

Supplemental Figure 6. Fluorescent *in situ* hybridization of *Tbx5*-dependent genes. (A-L') Fluorescent *in situ* hybridization at E14.5 after tamoxifen at E6.5 of *Nppa*, *Slit2* and *Ntn1* are expressed in the trabecular layer in *Tbx5*$^{CreERT2/+}$ controls (*Tbx5*$^{CreERT2/+}$;*Mef2cAHF-DreERT2*;*ROSA26*$^{Ai6/Ai66}$), and misexpressed in the IVS in *Tbx5*$^{CreERT2/flox}$ mutants (*Tbx5*$^{CreERT2/flox}$;*Mef2cAHF-DreERT2*;*ROSA26*$^{Ai6/Ai66}$) with a membranous VSD at E14.5. *Tnnt2* is expressed in cardiomyocytes.(M-X') Expression of *Bmp2*, *Robo1* and *Unc5b* are expressed in the atrioventricular canal (boxed region) in *Tbx5*$^{CreERT2/+}$ controls, and expression of these genes are reduced in *Tbx5*$^{CreERT2/flox}$ mutants.

Figure S7

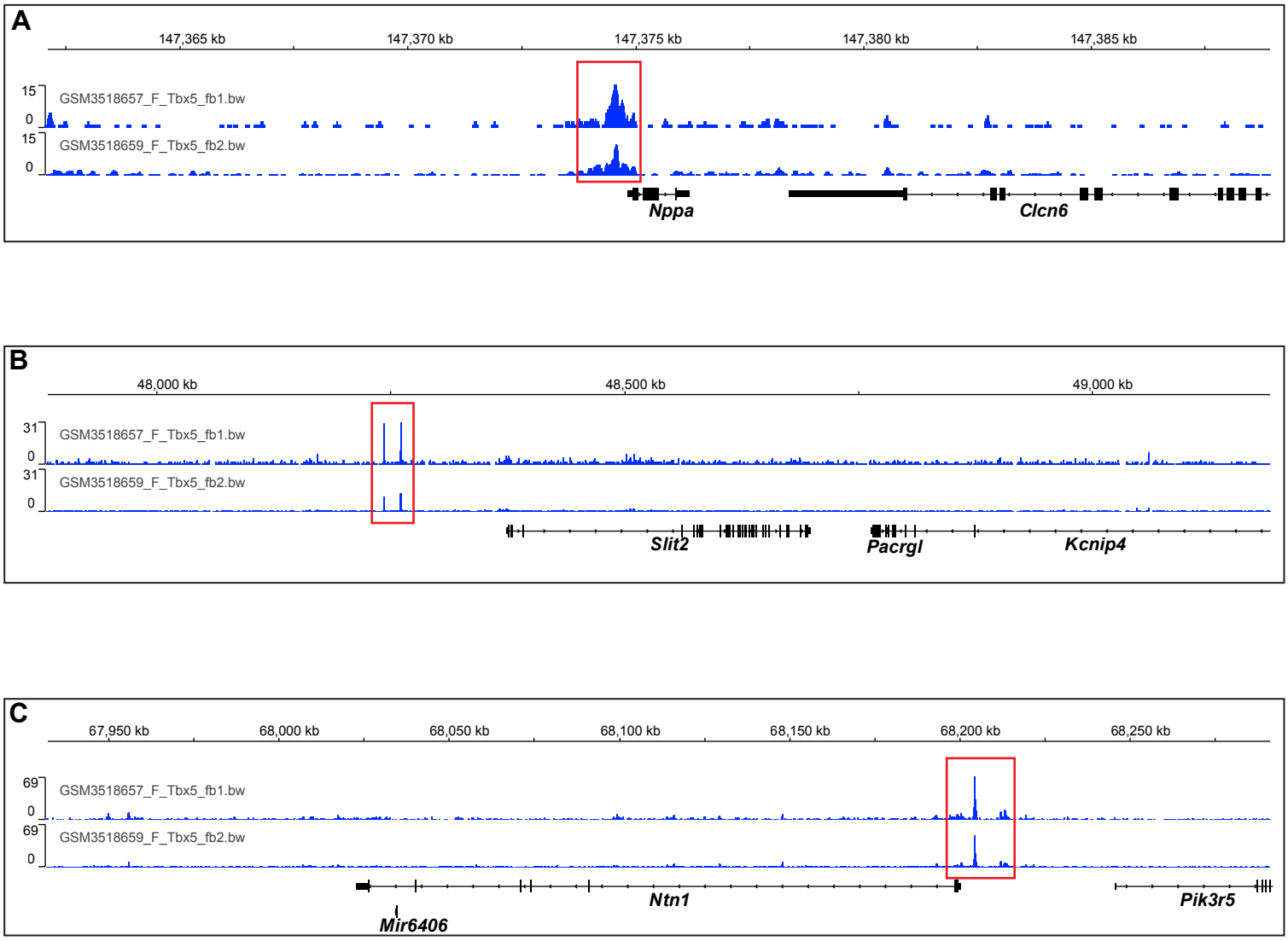
A
147,365 kb
147,370 kb
147,375 kb
147,380 kb
147,385 kb
15
0
GSM3518657_F_Tbx5_fb1.bw
15
0
GSM3518659_F_Tbx5_fb2.bw
Nppa
Clcn6
B
48,000 kb
48,500 kb
49,000 kb
31
0
GSM3518657_F_Tbx5_fb1.bw
31
0
GSM3518659_F_Tbx5_fb2.bw
Slit2
Pacrgl
Kcnip4
C
67,950 kb
68,000 kb
68,050 kb
68,100 kb
68,150 kb
68,200 kb
68,250 kb
69
0
GSM3518657_F_Tbx5_fb1.bw
69
0
GSM3518659_F_Tbx5_fb2.bw
Ntn1
Pik3r5
Mir6406

Supplemental Figure 7. TBX5 chromatin occupancy near *Slit2* and *Ntn1*. (A-C) Browser tracks of TBX5 ChIP-seq from E12.5 hearts (from Akerberg et al., 2019) shows peaks of TBX5 occupancy (boxed in red) near promoters of *Nppa*, *Slit2* and *Ntn1*.

Figure S8

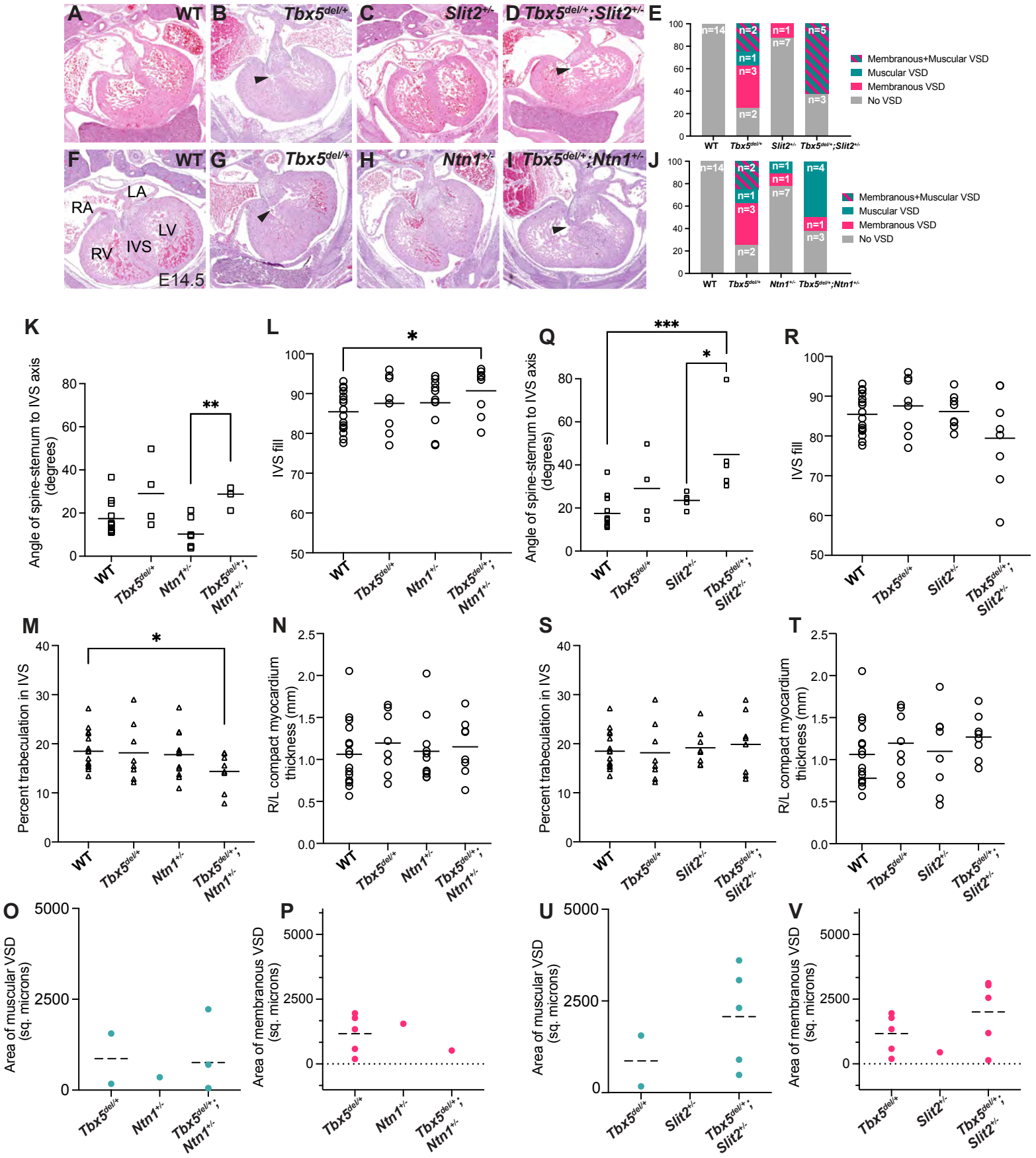
A WT
B Tbx5del/+
C Slit2+/-
D Tbx5del/+;Slit2+/-
E
F WT
G Tbx5del/+
H Ntn1+/-
I Tbx5del/+;Ntn1+/-
J
RA
LA
LV
RV
IVS
E14.5
Membranous+Muscular VSD
Muscular VSD
Membranous VSD
No VSD
K
L
Q
R
M
N
S
T
O
P
U
V
Angle of spine-sternum to IVS axis (degrees)
IVS fill
Percent trabeculation in IVS
R/L compact myocardium thickness (mm)
Area of muscular VSD (sq. microns)
Area of membranous VSD (sq. microns)
WT
Tbx5del/+
Ntn1+/-
Tbx5del/+; Ntn1+/-
Slit2+/-
Tbx5del/+; Slit2+/-

Supplemental Figure 8. *Tbx5-Slit2* and *Tbx5-Ntn1* genetic interactions. Histology from E14.5 embryos from matings of (A-D) *Tbx5*$^{del/+}$ and *Slit2*$^{+/-}$ or (F-I) *Tbx5*$^{del/+}$ and *Ntn1*$^{+/-}$ by genotype. Arrowheads depict muscular ventricular septal defects (VSDs). (E, J) Quantification of membranous or muscular VSDs by genotype. *Tbx5*$^{del/+}$;*Slit2*$^{+/-}$compound heterozygous embryos displayed an estimated decrease in the incidence of membranous VSDs, which approached significance (log OR -2.5; $p<0.09$ in a Generalized Linear Model). *Tbx5*$^{del/+}$;*Ntn1*$^{+/-}$ compound heterozygous embryos displayed a decrease of membranous VSDs (log OR -5.3; $p<1x10^{-3}$ by a Generalized Linear Model), but not changes to prevalence of muscular VSDs (log OR 0.12; $p<0.93$). Machine-learning based quantitative morphometry of metrics for (K-P) *Tbx5*$^{del/+}$ and *Ntn1*$^{+/-}$ or (Q-V) *Tbx5*$^{del/+}$ and *Slit2*$^{+/-}$ by genotype. IVS, interventricular septum. Significance determined by Fisher's exact test (*$p<0.05$, **$p<0.01$, ***$p<0.001$).

Figure 6

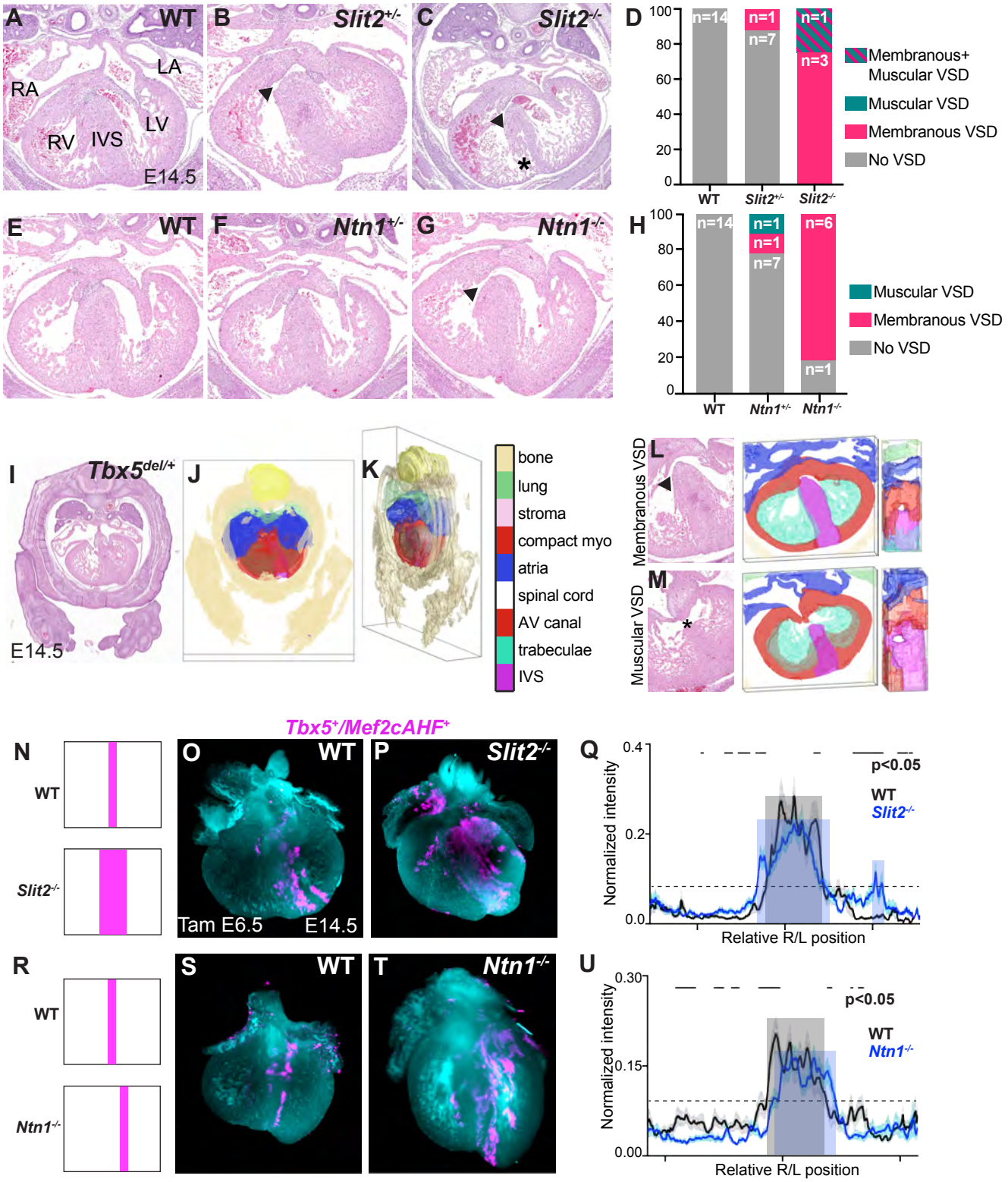
A
WT
RA
LA
RV
IVS
LV
E14.5
B
Slit2+/-
C
Slit2-/-
D
n=14
n=1
n=7
n=1
n=3
Membranous+ Muscular VSD
Muscular VSD
Membranous VSD
No VSD
WT
Slit2+/-
Slit2-/-
E
WT
F
Ntn1+/-
G
Ntn1-/-
H
n=14
n=1
n=1
n=7
n=6
n=1
Muscular VSD
Membranous VSD
No VSD
WT
Ntn1+/-
Ntn1-/-
I
Tbx5del/+
E14.5
J
K
bone
lung
stroma
compact myo
atria
spinal cord
AV canal
trabeculae
IVS
L
Membranous VSD
M
Muscular VSD
Tbx5+/Mef2cAHF+
N
WT
Slit2-/-
O
WT
Tam E6.5
E14.5
P
Slit2-/-
Q
Normalized intensity
p<0.05
WT
Slit2-/-
Relative R/L position
R
WT
Ntn1-/-
S
WT
T
Ntn1-/-
U
Normalized intensity
p<0.05
WT
Ntn1-/-
Relative R/L position

Figure 6. *Slit2* and *Ntn1* are essential for proper ventricular septation and compartment boundary regulation. (A-C) Histology and (D) incidence of muscular or membranous (arrowhead) ventricular septal defects (VSDs) of *Slit2* mutants are shown. Asterisk demarcates non-compacted interventricular septum (IVS) (E-G) Histology and (H) incidence of muscular or membranous ventricular septal defects (VSDs) of *Ntn1* mutants are shown. (I-K) Machine learning-based 3-D reconstructions of the embryonic heart and other tissues from histology at E14.5 were used for quantitative morphometric analysis of the embryonic heart (Supplemental Figure 7, Supplemental Figure 8). Compact myo, compact myocardium; AV canal, atrioventricular canal; IVS, interventricular septum. (L,M) A 3-D reconstruction of a membranous ventricular septal defect (VSD) anteriorly and muscular VSD posteriorly from a *Tbx5*$^{del/+}$ mutant heart. (N-P) Lightsheet imaging of *Slit2*$^{-/-}$ mutant (*Tbx5*$^{CreERT2/+}$;*Mef2cAHF-DreERT2*;*ROSA26*$^{Ai66/+}$;*Slit2*$^{-/-}$)(n=4) hearts at E14.5 showed a broadened distribution of the *Tbx5*$^{+}$/*Mef2cAHF*$^{+}$ lineage (tdTomato^{+} immunostaining) compared to controls (*Tbx5*$^{CreERT2/+}$;*Mef2cAHF-DreERT2*;*ROSA26*$^{Ai66/+}$;*Slit2*$^{+/+}$)(n=2), as (Q) quantified by linear profiles of fluorescence signals above a threshold (dashed line). Gray shading represents control signal above threshold, and periwinkle represents mutant signal. Significance of $p<0.05$ was determined by Welch's two-sample t-test at each position along the right-left axis. (R-T) Lightsheet imaging of *Ntn1*$^{-/-}$ mutant (*Tbx5*$^{CreERT2/+}$;*Mef2cAHF-DreERT2*;*ROSA26*$^{Ai66/+}$;*Ntn1*$^{-/-}$)(n=6) hearts at E14.5 showed a leftward shift in positioning of the *Tbx5*$^{+}$/*Mef2cAHF*$^{+}$ lineage compared to controls (*Tbx5*$^{CreERT2/+}$;*Mef2cAHF-DreERT2*;*ROSA26*$^{Ai66/+}$;*Ntn1*$^{+/+}$)(n=4), as (U) quantified by linear profiles.

Figure S9

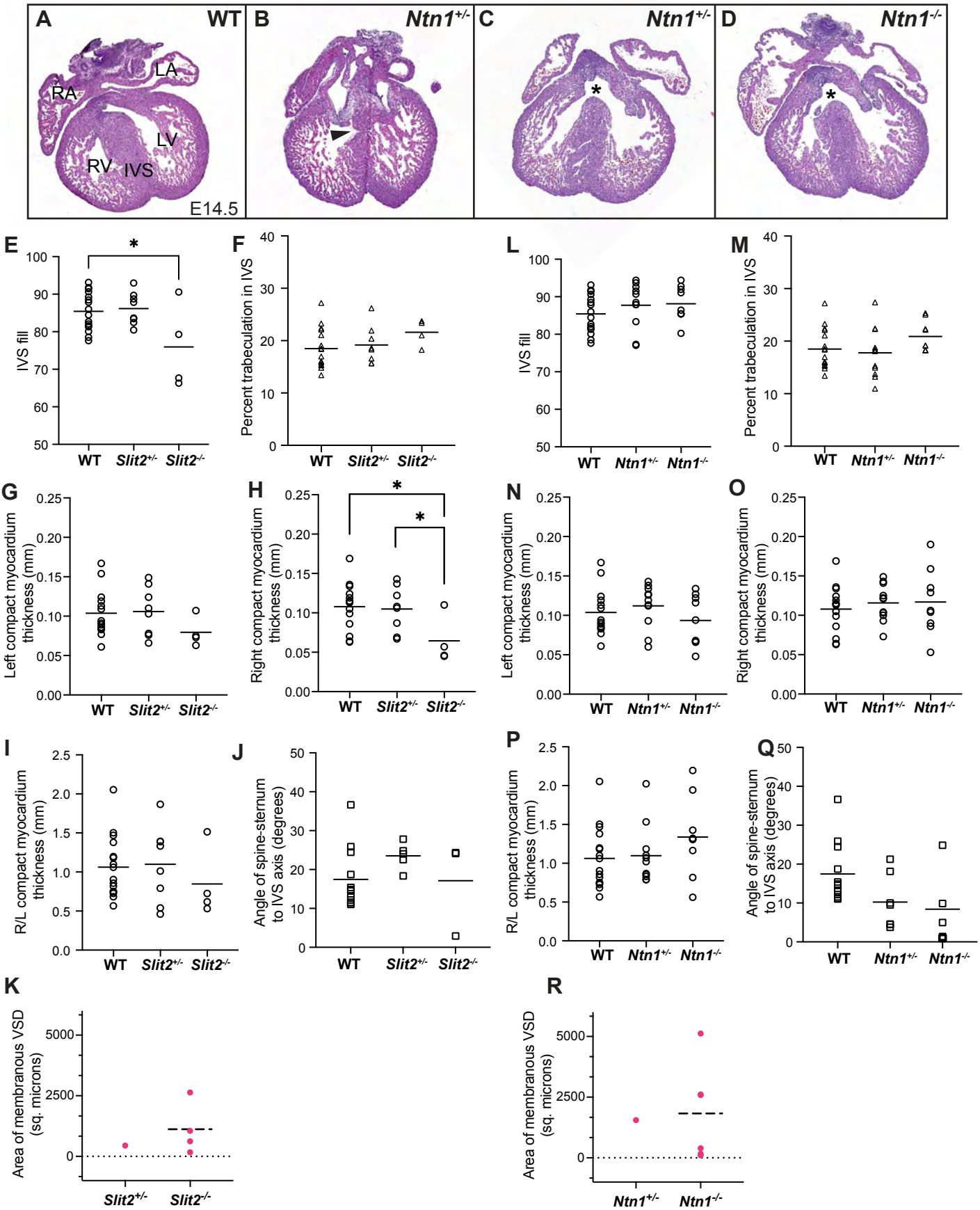
A
WT
LA
RA
LV
RV
IVS
E14.5
B
Ntn1+/-
C
Ntn1+/-
D
Ntn1-/-
E
IVS fill
WT
Slit2+/-
Slit2-/-
F
Percent trabeculation in IVS
L
Ntn1+/-
Ntn1-/-
M
G
Left compact myocardium thickness (mm)
H
Right compact myocardium thickness (mm)
N
O
I
R/L compact myocardium thickness (mm)
J
Angle of spine-sternum to IVS axis (degrees)
P
Q
K
Area of membranous VSD (sq. microns)
R

179 **Supplemental Figure 9. Quantitative morphometry of *Slit2* and *Ntn1* mutant hearts.** (A-D)
180 Additional histology by *Ntn1* genotype. Arrowhead, muscular ventricular septal defect (VSD).
181 Asterisk, membranous VSD. (E-P) Machine learning-based quantitative cardiac morphometrics
182 for (E-K) *Slit2* or (L-R) *Ntn1* mutants. Significance determined by Fisher's exact test (*$p<0.05$).
183 (Q,R) Morphometry of the area of membranous VSDs by *Slit2* or *Ntn1* genotypes.
184